Микроелектроника
и оптоелектроника

Microelectronics
and optoelectronics

Response Surface Methodology and Artificial Neural Network-Based Models for Predicting Roughness of Cu coatings

Ivana Mladenović, Jelena Lamovec, Nebojša D. Nikolić, Stevan Andrić, Marko Obradov, Vesna Radojević, Dana Vasiljević-Radović

***Abstract*— Copper coatings are produced on silicon wafer by electrodeposition (ED) in pulsating current (PC) regime. Electrodeposition was performed at various current density amplitudes in the range of 80–140 mA cm^{-2}, frequency in the range of 30–100 Hz and coating thickness in the range of 10–60 μm. The resulting composite systems consist of monolayered copper films electrodeposited from sulfate bath on Si wafers with sputtered layers of Cr/Au. Roughness measurements were performed to evaluate properties of the copper coating surface. The coating roughness (R) was measured using Atomic Force Microscope in contact mode. The software Gwyddion was used for determination an average roughness parameter (R_a). After that (Artificial Neural Network-ANN) model was used to study the relationship between the parameters of electrodeposition process and roughness of copper coatings. The influence of experimental values: amplitude current density, frequency and thickness of coating on the surface roughness will be highlighted. Response surface methodology (RSM) was utilized to improve the correction between R_a and input parameters. Finally, the results of the average roughness (experimental and predicted) were used to estimate the new value of (Ra) of copper for each variation of the input parameters and compared capability of ANN and regression analysis for surface roughness generated under different electrochemical conditions. The coefficient of determination was found 92% for ANN and 93% for regression analysis.**

***Index Terms*—electrodeposition, roughness, AFM, coatings, ANN, RSM.**

Ivana Mladenović is with Institute of Chemistry, Technology and Metallurgy, University of Belgrade, Njegoševa 12, Belgrade, Serbia (e-mail: ivana@nanosys.bg.ac.rs).

Jelena Lamovec is with Institute of Chemistry, Technology and Metallurgy, University of Belgrade, Njegoševa 12, Belgrade, Serbia (e-mail: jejal@nanosys.bg.ac.rs).

Nebojša D. Nikolić is with Institute of Chemistry, Technology and Metallurgy, University of Belgrade, Njegoševa 12, Belgrade, Serbia (e-mail: nnikolic@ihtm.bg.ac.rs).

Stevan Andrić is with Institute of Chemistry, Technology and Metallurgy, University of Belgrade, Njegoševa 12, Belgrade, Serbia (e-mail: stevan@nanosys.bg.ac.rs).

Marko Obradov is with Institute of Chemistry, Technology and Metallurgy, University of Belgrade, Njegoševa 12, Belgrade, Serbia (e-mail: marko.obradov@nanosys.bg.ac.rs).

Vesna Radojević is with the Faculty of Technology and Metallurgy, University of Belgrade, Karnegijeva 4, 11 000 Belgtrade, Serbia (e-mail: vesnar@tmf.bg.ac.rs).

Dana Vasiljević-Radović is with Institute of Chemistry, Technology and Metallurgy, University of Belgrade, Njegoševa 12, Belgrade, Serbia (e-mail: dana@nanosys.bg.ac.rs).

I. INTRODUCTION

Electrodeposition is one of the methods for developing nanocrystalline copper thin coatings with variation surface quality depending on the deposition parameter and the properties of the substrate.

The best benefit of electrodeposition process over other metallization methods such as chemical or physical vapor deposition (CVD or PVD) is speed, simplicity, low cost and the ability to predefine material properties as a function of variable of electrodeposition conditions.

For application in Micro-Electro-Mechanical Systems (MEMS) technologies, coatings must have satisfactory properties such as: good wear and corrosion resistance, compactness, fine microstructure, strong adhesion to the substrate, good mechanical durability and ductility and low roughness [1-5]. The surface roughness is an important indicator of the quality of electrodeposited metallic coatings. Also, the mechanical properties, such as microhardness [4], creep life and fatigue behavior [6] and electrical properties like conductivity [7] depend on the surface roughness of the coatings.

Measuring the surface roughness of a coating by scanning microscopy, such as AFM is a time-consuming process as is the processing of each individual image, but is a starting point for collecting of the roughness data, necessary to monitor the quality of the coatings.

By the use of the developed software package, we are able to design an experiment, predictable behavior of materials with variation of process parameters and generate a model that best describes the system we designed.

Artificial neural network (ANN) is powerful tools for modeling, especially when the data are randomly distributed and when the connection between the input parameters is unknown [8-10]. Response Surface Methodology (RSM) represents a collection of mathematical and statistical techniques that are useful for the modeling, analysis data sets and find the mathematical correlation between the input variables and the output response [11-12].

Both methods (ANN and RMS) can be used to predict the values of output variables (mainly the measured values) as a function of input variables (process parameters) depending on

the type of system and the quality of prediction we want to achieve [13].

II. Experimentation

2.1. Materials and experimental conditions

Electrodeposition of copper was performed from sulfate bath, composition: 240 g /L $CuSO_4 \cdot 5 H_2O$, 60 g /L H_2SO_4. The deposition was performed in an open-type cell at the room temperature by the regime of pulsating current (PC).

The parameters of the PC regime used in the processes of electrodeposition are given in Table 1. The current density amplitude (j_A in mA cm^{-2}), frequency (f in Hz) and coating thickness (δ in μm) are varied parameters. Deposition pulse time (t_c in ms) was kept constant at 5 ms.

TABLE I: Deposition Parameters.

No.	j_A/ mAcm^{-2}	f/ Hz	δ/ μm
1	80	100	40
2	100	100	40
3	120	100	40
4	140	100	40
5	100	30	40
6	100	50	40
7	100	80	40
8	100	100	10
9	100	100	20
10	100	100	60

For these experiments, substrate of Si wafers (2'', (111) orientation) was chosen and prepared to serve as a cathode. The wafer was cut in parts (1 × 1) cm^2 surface area, standard cleaning and drying procedures. The plating base on the silicon wafers were sputtered layers of 30 nm Cr and 100 nm Au, using Perkin Elmer 2400 sputtering system. High purity copper was used as an anode.

2.2. Roughness measurement of copper coatings

The surface topography and roughness of the Cu coatings were examined using atomic force microscope (AFM, TM Microscopes-Vecco) in the contact mode. The values of the arithmetic average of the absolute roughness parameters (R_a) of the surface height deviation, were measured from the mean image data plane, using software Gwyddion. The values of R_a roughness parameter, calculated as average from three independent measurements at different locations of one sample of copper surface obtained by the PC regime with variation of electrodeposition conditions. For three different scan areas (2500, 4900 and 8100) μm^2, two measurements were made, and average roughness parameter was calculated.

The average roughness can be calculated as:

$$R_a = \frac{1}{N_x \cdot N_y} \sum_{i=1}^{N_x} \sum_{j=1}^{N_y} \left| z(i,j) - z_{mean} \right| \quad (1)$$

where N_x and N_y are the number of scanning points on the x-axis and y-axis; z(i,j) is the height of the (i,j) measuring point, z_{mean} is the mean high of all measuring points [14].

III. Results and Discussion

The AFM surface areas of Cu coatings produced at different thickness (10 and 60 μm) are shown in Fig. 1. The values of R_a parameter obtained for various thickness of coatings for three scan area surface area are shown in Table II.

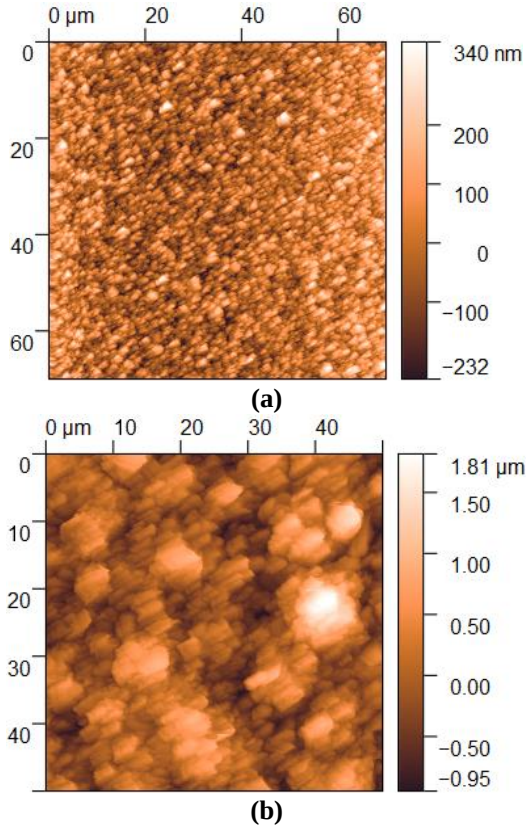

Fig. 1. The AFM images of Cu coatings obtained by the PC regimes: a) δ = 10 μm, b) δ = 60 μm. j_A= 100 mA cm^{-2}, f = 100 Hz, t_c = 5 ms. Scan area was 2500 μm^2.

TABLE II
Roughness variation with coating thickness and constant frequency and amplitude current density; j_A =100 mA cm^{-2} and f = 100 Hz.

δ/ μm	***Scan area***/ μm × μm	***Ra***/ nm	***δ***/ μm	***Scan area***/ μm × μm	***Ra***/ nm
10	50 × 50	66.54	20	50 × 50	114.7
10	50 × 50	65.12	20	50 × 50	121.9
10	70 × 70	65.81	20	70 × 70	121.2
10	70 × 70	60.82	20	70 × 70	120.4
10	90 × 90	64.71	20	90 × 90	125.9
10	90 × 90	74.99	20	90 × 90	119.7
40	50 ×50	280.8	60	50 × 50	299.9
40	50 × 50	277.9	60	50 × 50	325
40	70 × 70	249.3	60	70 × 70	309.4
40	70 × 70	246.6	60	70 × 70	309.2
40	90 × 90	247.1	60	90 × 90	297.5
40	90 × 90	251.6	60	90 × 90	292.9

3.1 Artificial Neural Network (ANN)

MATLAB R2017b and *nntool* box was chosen and applied on roughness experimental data for training, testing, validation and prediction of new values of R_a. In the present work, feedforward back propagation network was utilized. The best network structure for this set data was 4-10-1, 4 corresponding to the input layer neurons, 10 to hidden layer neurons and 1 to output layer neurons. The numerical technique for optimization was Levenberg-Marquardt (LM).

The plot on Fig. 2 shows a regression between network outputs and network targets. If the training were perfect, the network outputs and the targets would be equal. The R-values were found as 0.99608 for training (Fig. 2a), 0.99636 for validation (Fig. 2b), 0.99176 for testing (Fig. 2c) and 0.99553 for all data set (Fig. 2d).

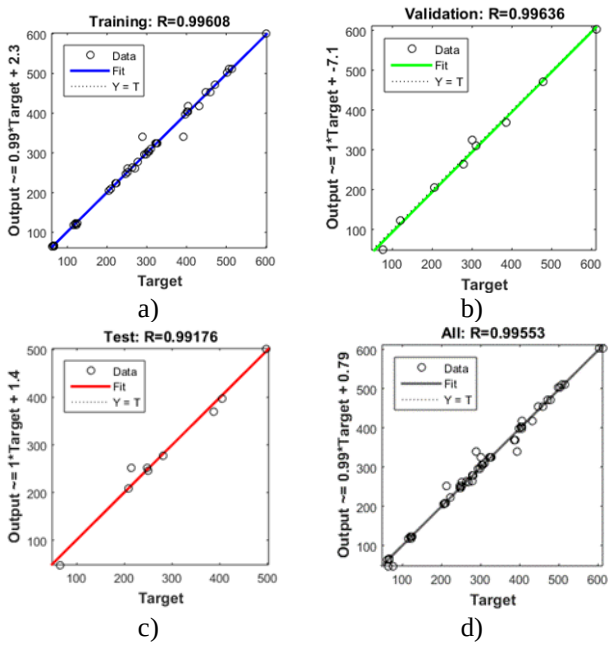

Fig. 2. The ANN regression for roughness parameter modeling, a) training data (70% of data set), validation data (15%) and testing (15%).

Based on the values of the regression coefficient values (R) and values of the mean relative error (MRE) ANN predictive model is satisfactory and adequate. Fig. 3 shows the experimental and the corresponding ANN predicted values as well as the relative error for each data. The mean absolute percentage error (MAPE) for the ANN model was 7.84 %, calculated from the data in Fig. 3.

The maximal error was detected for sample with lower scanned area, which was expected due to the sensitivity of the measurement method. For a realistic estimation of the roughness of the samples it is necessary to make measurements at different locations of the sample and at different scanned surfaces.

3.1 Response Surface Methodology (RSM)

Design-Expert 12 software and response surface central-composite-design was employed for experimental design. A small data set was used, for a constant scan area value of 2500 μm^2 for all samples. The factors and factor levels are shown in Table III.

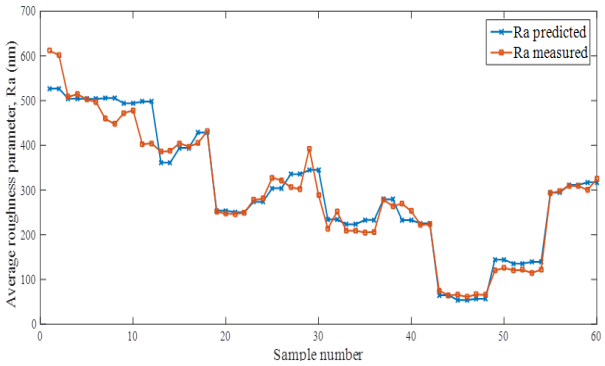

Fig. 3. Experimental versus predicted values of surface roughness using ANN.

TABLE III The factors levels.

Factors	Levels			
Amplitude of current density	80	100	120	140
Frequency	30	50	80	100
Coating thickness	10	20	40	60

The analysis of variance (ANOVA) was utilized in testing the roughness data. The linear-model generated by the following equation:

$$Y_u = \beta_0 + \sum_{i=1}^{n} \beta_i x_i + e \qquad (2)$$

where Y_u is the required response, β_0, β_1... β_i are the regression coefficients, x is the independent variables and e is the error.

The final equation in terms of coded factors is given as:

$$R_a = 506.9598 - 1.11778\, j_A - 3.63598\, f + 5.39583\, \delta \qquad (3)$$

The equation (3) can be used to make predictions about the response for given levels of each factor. By default, the high levels of the factors are coded as +1 and the low levels are coded as -1. The coded equation is useful for identifying the relative impact of the factors by comparing the factor coefficients. We can see that thickness is dominated factor on influence to the roughness copper coatings. Fig. 4 shows the residuals against run test and data points are randomly distributed.

Fig. 5 shows the predicted response vs. the actual value points are distributed along a 45° line; this means that the organized model is adequate and satisfactory.

Fig. 6 is a 3D view response surface curve for surface roughness. The best roughness value can be obtained at 100 Hz with current density at 100 mA cm^{-2}, for small coating thickness.

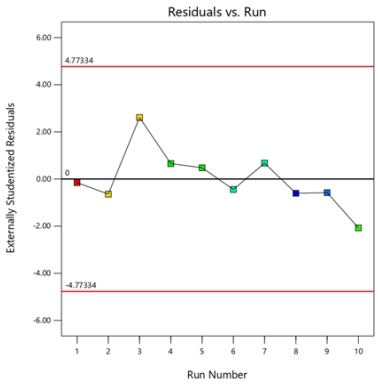

Fig. 4. Residuals against run tests for surface roughness parameter.

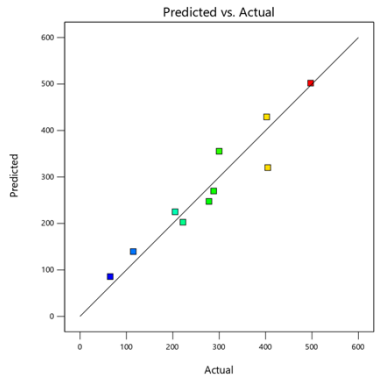

Fig. 5. Predicted response *vs*. the actual values for surface roughness parameter for copper coatings.

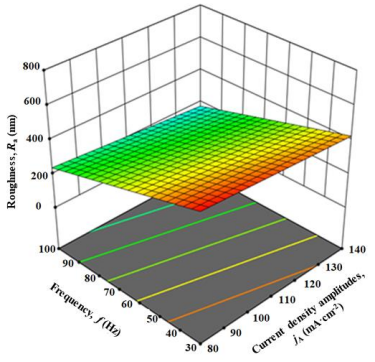

Fig. 6. 3D response surface curves for the surface roughness. A coating thickness of 35 μm was selected for prediction.

IV. Conclusion

The conditions suitable for formation of compact and uniform Cu coatings of a satisfactory roughness by the regime of pulsating current (PC) were defined. The Cu coatings were obtained with variation of an amplitude of current density, frequency and coating thickness. The minimal roughness showed the Cu coatings obtained at 100 Hz with the current density amplitude of 100 mA cm^{-2} and coating thickness at 10 μm. From the results obtained by application of two different models follows:

-The coating thickness has strong influence on micro roughness;

-The current density also strongly affected the coating roughness, but less than frequency.

-Both RSM and ANN show good agreement with experimental results.

-Both methods can be effectively used to predict coating roughness.

Acknowledgment

This work was financially supported by the Ministry of Education, Science and Technological Development of the Republic of Serbia (Grants No. 451-03-68/2020-14/200026 and No. 451-03-68/2020-14/200135).

References

[1] A. Maciossek, B. Lochel, H. J. Quenzer, B. Wagner, S. Schulze, J. Noetzel, "Galvanoplating and sacrificial layers for surface micromachining", *Microelectron. Eng.* , vol. *27*, no.*1*, pp. *503-508*, Feb., 1995.

[2] Z. Zhao, L. Du, Z. Xu, L. Shao, "Effects of ultrasonic agitation on adhesion strength of micro electroforming Ni layer on Cu substrate," *Ultrason. Sonochem.*, vol. *29*, no./, pp. *1-10*, Mar., 2016.

[3] S. Banthia, S. Sengupta, S. Das, K. Das, "Cu, Cu-SiC functionally graded coating for protection against corrosion and wear", *Surf. Coat. Technol.*, vol. *374*, no. , pp. *833-844*, Sept., 2019.

[4] I. Mladenović , J. Lamovec, V. Jović, M. Obradov, D. Vasiljević-Radović, N. D. Nikolić, V. Radojević, "Mechanical characterization of copper coatings electrodeposited onto different substrates with and without ultrasound assistance", *J. Serb. Chem. Soc.* , vol. *84*, no. *7*, pp.*729-741*, Mar., 2019.

[5] J.B. Marro, T. Darroudi, C.A. Okorod, Y.S. Obeng, K.C. Richardson, "The influence of pulse plating frequency and duty cycle on the microstructure and stress state of electroplated copper films", *Thin Solid Films*, vol. *621*, no. , pp. *91–97*, Jan., 2017.

[6] B. Wilshire, A.J. Battenbough, "Creep and creep fracture of polycrystalline copper", *Mater. Sci. Eng. A*, vol. *443*, no./, pp. *156-166*, Aug., 2007.

[7] A. Javidjam, M. H. Hekmatshoar, L. Hedayatifar, S. N. K. Abad, "Effect of surface roughness on electrical conductivity and hardness of silver plated copper", *Mater. Res. Express*, vol. *6*, no. *3*, pp. *036407*, Dec., 2019.

[8] I. Mladenović, J. Lamovec, V.Jović, M. Obradov, K. Radulović, D. Vasiljević-Radović, V. Radojević, "Artificial Neural Network for Composite hardness Modeling of Cu/Si Systems Fabricated Using Various Electrodeposition Parameters", Proc. of the 31th International Conference on Microelectronics MIEL, Niš, Serbia, pp. 133-136, 16.-18. Sept., 2019.

[9] D. M. Habashy, H. S. Mohamed, E. F. M. El-Zaidia, "A simulated neural system (ANNs) for micro-hardness of nano-crystalline titanium dioxide", *Physica B: Condensed Matter*., vol. *556*, pp.*183-189*, Mar., 2019.

[10] M.S. Ozerdem, S. Kolukisa, "Artificial neural network approach to predict the mechanical properties of Cu-Sn-Pb-Zn-Ni cast alloys", *Materials and design*, vol. *30*, no. *3*, pp.*764-769*, Mar., 2009.

[11] G. Orhan, G. Hapci, O. Keles, "Application of Response Surface Methodology (RSM) to Evaluate the Influence of Deposition Parameters on the Electrolytic Cu-Zn Alloy Powder", *Int. J. Electrochem. Sci.* , vol. *6*, no. , pp. *3966-3981*, Sept. , 2011.

[12] V. Ponraj, A.Azhagurajn, S. C. Vettivel, S. Shajan, P. Y. Nabhiraj, A. Haiterlenin, "Modeling and Optimization of the Effect of Sintering Parameters on the Hardness of Copper/Graphene Nanosheet Composites by Response Surface Methodology" , *Met. Sci. Heat Tret.*, vol. *60*, no. *9*, pp. *611-615*, Mar., 2019.

[13] A. A. Elsadek, A. M. Gaafer, S.S. Mohamed, "Surface roughness prediction in hard-turning with ANN and RSM", Journal of the Egyptian society of Tribology, vol. *17*, no. *2*, pp. *13-22*, Apr., 2020.

[14] Y. Li, J. Yang, Z. Pan, W. Tong, "Nanoscale pore structure and mechanical property analysis of coal: An insight combining AFM and SEM images", *Fuel*, vol. 260, no. , pp. *116352*, Jan., 2020.

Influence of sintering temperature on the performance of titanium dioxide anode in Dye Sensitized Solar Cells with natural pigment hypericin

Katarina Cvetanović Zobenica, Nenad Tadić, Uroš Lačnjevac, Evgenija Milinković, Milena Rašljić Rafajilović, Milče M. Smiljanić, Dana Vasiljević-Radović, Dragomir Stanisavljev

***Abstract*—Dye Sensitized Solar cells (DSSC) are very attractive due to their low cost fabricating methods and used materials. One of the most important parts of the cells is the photoanode. Many semiconducting materials are used for this purpose, but most common one is titanium dioxide (TiO_2). Optimal sintering temperature of anode plays important role in performance of TiO_2 layer in DSSC, since it provides good electrical contact between particles, which consequently leads to better electron transfer through the cell, but still restricts unfavorable phase transformation. In this paper two identical cells with natural pigment hypericin as sensitizer were assembled with anodes sintered on two different temperatures (500 °C and 600 °C), so their performance parameters could be compared. The ratios between the maximal power densities (P_{max}) and solar to electrical energy conversion efficiencies (η) for the two measured cells are 5 times in favor for the cell sintered at 600 °C, which shows the importance of temperature treatment of TiO_2 electrodes for better performance of solar cells.**

***Index Terms*— DSSC; TiO_2 anode; sintering temperature; hypericin.**

I. Introduction

Dye-sensitized solar cells (DSSC) are very popular due to a low cost of production materials and methods, compared to silicon-based solar cells. They were first introduced in 1991[1] and since then, their performance has been improving [2-4].

The operating principle of DSSC is very simple, as presented in Fig 1. It is designed to mimic photosynthesis in plants. Incident solar photon oxidizes the sensitizer, which further delivers the electron to conduction band of semiconductor. Dye molecule then gets reduced by electrolyte, and electrolyte is further regenerated at the counter electrode. Most common electrodes for DSSC are TiO_2 for anode, and platinum electrode as counter one. Widely used electrolyte is I^-/I_3^- solution in acetonitrile[5].

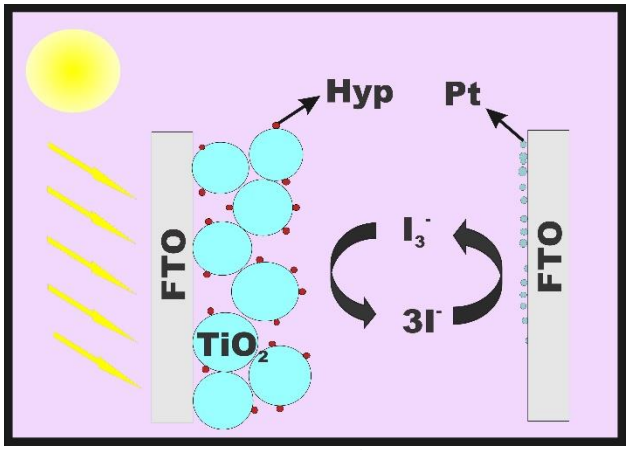

Fig. 1. Schematic representation of DSSC constituent parts

Many types of sensitizers are known and used today: organic, inorganic, synthetic, natural [5]. DSSCs with porphyrin and ruthenium dyes have the highest efficiency of conversion solar energy into electrical, reaching 11 and 13 % [6]. The price and toxicity are great disadvantages of these dyes [7]. On the other hand, natural pigments extracted from flowers, plants and fruits are affordable and widespread, but their efficiency of conversion is only a few percent [8]. The best result published so far for natural pigment sensitized solar cell reported Ghann [9] with pomegranate juice and reached the efficiency of 2 %. In the extensive study by Kumara [10], the best performance showed red turnip, and

Katarina Cvetanović Zobenica is with the University of Belgrade – Institute of Chemistry, Technology and Metallurgy – National Institute of the Republic of Serbia, Njegoševa 12, 11000 Belgrade, Serbia (e-mail: katarina@nanosys.ihtm.bg.ac.rs).

Nenad Tadić is with the Faculty of physics, University of Belgrade, Studentski trg 12, 11000 Belgrade, Serbia (e-mail: nenad.tadic@ff.bg.ac.rs).

Uroš Lačnjevac is with the Institute for Multidisciplinary Research, University of Belgrade, Kneza Višeslava 1, 11030 Belgrade, Serbia (e-mail: uros.lacnjevac@imsi.bg.ac.rs).

Evgenija Milinković is with the University of Belgrade – Institute of Chemistry, Technology and Metallurgy – National Institute of the Republic of Serbia, Njegoševa 12, 11000 Belgrade, Serbia (e-mail: evgenija@nanosys.ihtm.bg.ac.rs).

Milena Rašljić Rafajilović is with the University of Belgrade – Institute of Chemistry, Technology and Metallurgy – National Institute of the Republic of Serbia, Njegoševa 12, 11000 Belgrade, Serbia (e-mail: milena@nanosys.ihtm.bg.ac.rs).

Milče M. Smiljanić is with the University of Belgrade – Institute of Chemistry, Technology and Metallurgy – National Institute of the Republic of Serbia, Njegoševa 12, 11000 Belgrade, Serbia (e-mail: smilce@nanosys.ihtm.bg.ac.rs).

Dana Vasiljević-Radović is with the University of Belgrade – Institute of Chemistry, Technology and Metallurgy – National Institute of the Republic of Serbia, Njegoševa 12, 11000 Belgrade, Serbia (e-mail: dana@nanosys.ihtm.bg.ac.rs).

Dragomir Stanisavljev is with the Faculty of physical chemistry, University of Belgrade, Studentski trg 12, 11000 Belgrade, Serbia (e-mail: dragisa@ffh.bg.ac.rs).

reached cell efficiency was 1,70 % on 470 nm. Still, review papers show that most natural pigments have low performance, with conversion efficiency somewhere between 0,013 and 0,50 % [9].

Hypericin is a photosensitive pigment which is one of the principal active constituents of St. John's wort (Hypericum perforatum). Hypericin is novelty in terms of photovoltaics [11], although it is widely used for its photodynamical and phototherapeutic properties in medicine [12]. Hypericin's molecular structure is presented in Fig.2.

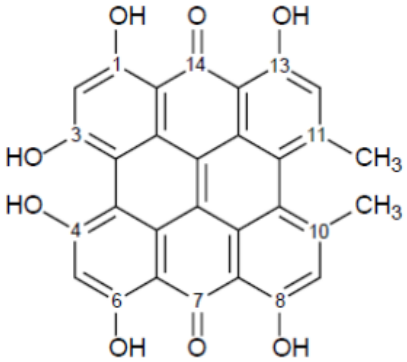

Fig 2.Molecular structure of hypericin.

TiO_2 is a stable, nontoxic oxide, which has a high refractive index (2.4-2.5) and naturally occurs in several crystal forms: rutile, anatase, and brookite. Rutile is the thermodynamically most stable form. Anatase is, however, the preferred structure in DSSCs, because it has a larger bandgap (3.2 vs 3.0 eV for rutile). In recent years, the progress has been made in the development of methods to synthesize new anatase nanostructures such as nanoparticles, nanorods, nanowires and nanotubes [13, 14]. These methods include sol-gel, micelle and inverse micelle, hydrothermal, electrodeposition and many more. One of the most important parameters of fabrication of TiO_2 anode is temperature of sintering, it provides good electrical contact between TiO_2 particles, while, carefully chosen, it does not allow phase transformation from anatase to rutile (~500 ºC) [15].

The goal of this paper is to compare the performance of two cells, almost identical, with the difference only in sintering temperature of anode, one at 500 °C, and the other at 600 °C. The motive can be found in the fact that the temperature of 500 °C is recommended as optimal for anatase electrode preparation, but the DSSC devices showed better performance when TiO_2 was sintered at 600 °C, although it showed phase transformation to rutile [16].

II. Experimental

TiO_2 paste was prepared as described by Ito in ref. [17]. TiO_2 powder (P25, Sigma) was transferred into alumina mortar and grinded, with addition of acetic acid, water and ethanol, respectively. After the transfer into the beaker with ethanol, it was stirred with a magnetic tip and sonicated with an ultrasonic horn. After this set of treatments, terpineol was added, and the mixing and sonication procedure was repeated. Then, the ethyl cellulose was added, and the sonication treatment was performed once more. At the end, the paste was evaporated from solvents.

TiO_2 paste was coated onto fluorine doped thin oxide glass (FTO), previously cleaned and treated with UV lamp and $TiCl_4$ treatment, by screen-printing. The photoanodes were then gradually heated under an airflow at 325 °C for 5 min, at 375 °C for 5 min, at 450 °C for 15 min and 500 °C for 15 min. One more step was performed on the electrode sintered at higher temperature – 600°C for 30 min. The exact temperature at the sample position was measured with a K-type thermocouple, Ni/NiCr.

The thickness of the TiO_2 layer was measured on comparator Iskra NP37 (15 µm).

X-ray diffraction (XRD) measurements were performed. (phase composition) using Rigaku Ultima IV X-ray diffraction instrument in thin film geometry with grazing incidence angle of 0.5°, using Ni-filtered CuKα radiation (λ = 1.54178 Å). Obtained data was analyzed with PDXL 2 software. Afterwards, the $TiCl_4$ treatment was conducted once again on TiO_2 anodes. Right after programmed heating to 500 ºC/600 ºCand cooling at 80 ºC, the electrode was immersed into 10^{-4} M hypericin solution in acetone and kept at room temperature for 20 h.

The counter electrode was prepared on cleaned FTO glass, and treated with a solution of HCl in ethanol. Then, after heating at 400 ºC a drop of H_2PtCl_6 solution in ethanol was applyed and heated under an airflow again at 400 ºC [17]. I^-/I_3^- electrolyte solution in acetonitrile was also prepared.

TiO_2 electrode, sensitized with hypericin, counter Pt electrode were assembled as a sandwich type cell with the sealing tape. A drop of electrolyte was put onto the hole on the Pt counter electrode, and then the cells were ready for measurements.

Photovoltaic characteristics of DSSC were examined with the solar simulator Abet, LS series 10500 at 1.5 AM, at 23˚C (measured with IR thermometer) controlled with circular thermostat Julabo F12 (under illumination).

Illumination of the system produces additional heat, so the assembled solar cell was thermostated at the steady state temperature of 23 ± 1 ºC. After achieving steady state temperature, photovoltaic measurement was performed by Gamry electrochemical devise, Gamry Series G 300 potentiostat, with Linear sweep voltammetry (LSV).

III. Results

The aim of this research was to investigate the influence of sintering temperature of TiO_2 layer on the performance of DSSCs with hypericin. Two identically prepared TiO_2 anodes were sintered at different temperatures—500 and 600 °C.

As seen in Fig. 3., XRD patterns of the two anodes feature three different peaks, from left to right: anatase form, substrate and rutile phase. The XRD measurements were performed to ensure that the majority of crystalline form is anatase, which was proven as better choice for DSSC than rutile even at 600 °C.

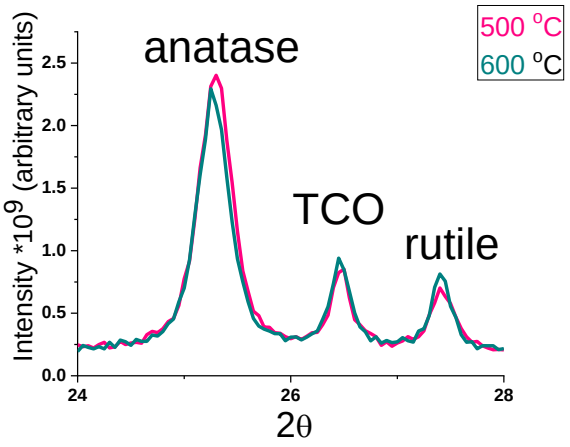

Fig. 3. Fractions of different crystal phases of TiO_2 and substrate TCO, sintered at 500 and 600 °C.

Current density–voltage curves for the cells with anodes sintered at two different temperatures are presented in Fig. 4 and Fig. 5.

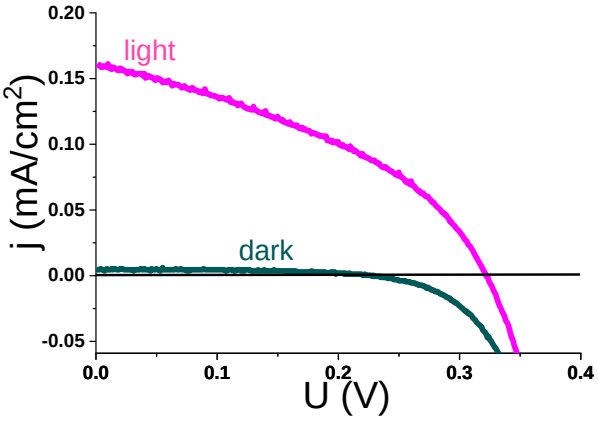

Fig.4. Current density–voltage characteristics of the cell sintered at 500 °C in the dark and under 100 mW cm^{-2} of simulated AM1.5 illumination for the illuminated device.

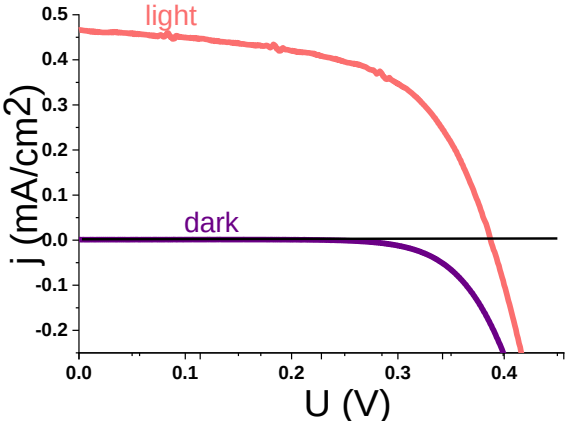

Fig.5. Current density–voltage characteristics of the cell sintered at 600 °C in the dark and under 100 mW cm^{-2} of simulated AM1.5 illumination for the illuminated device.

Comparing Fig. 4 and 5 it is noticeable, that the cell with the anode sintered at the higher temperature has far better performance. It has higher values for short circuit current density (j_{sc}) and open circuit voltage (U_{oc}). For better insight, the cells' performance parameters are given in Table 1 bellow.

TABLE I
IE CURVES PARAMETERS FOR MEASURED CELLS

	500 °C	600 °C
j_{sc} (mA/cm^2)	0.162	0.468
U_{oc} (mV)	322	387
P_{max} (μW/cm^2)	20.7	106.1
FF	39.7	58.6
η (%)	0.021	0.106

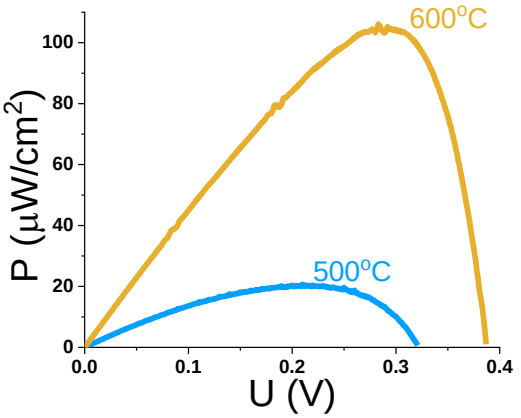

Fig.6. Power density-voltage characteristics of the cells sintered at 500 °C and 600 °C under 100 mW cm^{-2} of simulated AM1.5 illumination.

The ratios between the maximal power densities (P_{max}) and solar to electrical energy conversion efficiencies (η) for the two measured cells are 5 times in favor for the cell sintered at 600 °C, as seen in Fig. 6. It shows the importance of temperature treatment of TiO_2 electrodes for better performance of solar cells.

IV. Conclusion

The goal of this work was to present the importance of sintered temperature for an adequate performance of TiO_2 electrodes in dye sensitized solar cells. Two identical cells, with natural pigment hypericin as sensitizer and different sintered temperature were compared. The result showed five times higher value of maximal power density for the cell with the higher sintering temperature of 600 °C at given conditions. Despite that much lower temperature of electrode preparation is recommended in literature, obtained results show that anatase phase may be preserved even at much higher temperatures, depending of heating procedure. The reason for better performance of the cell treated with higher temperature is better electrical contact between TiO_2 particles, which provided better electron transfer through the anode, and

therefore lower resistance of the cell. This experiment was conducted on P25 TiO_2 particles, but it would be interesting to observe and compare optimal sintering temperatures for other nanostructures such as nanoparticles, nanorods, nanowires, nanotubes, etc.

ACKNOWLEDGMENT

This was financially supported by the Ministry of Education, Science and Technological Development of the Republic of Serbia (Grant No. 451-03-68/2020-14/200026 and OI172015).

REFERENCES

[1] B. O'Regan and M. Gratzel, "A low-cost, high-efficiency solar cell based on dye-sensitized colloidal TiO2 films," *Nature*, vol. 353, pp. 737-740, 1991.

[2] M. Grätzel, "Dye-sensitized solar cells," *Journal of Photochemistry and Photobiology C: Photochemistry Reviews*, vol. 4, pp. 145-153, 2003.

[3] J. Gong, K. Sumathy, Q. Qiao, and Z. Zhou, "Review on dye-sensitized solar cells (DSSCs): Advanced techniques and research trends," *Renewable and Sustainable Energy Reviews*, vol. 68, Part 1, pp. 234-246, 2017.

[4] C.-P. Lee, R. Y.-Y. Lin, L.-Y. Lin, C.-T. Li, T.-C. Chu, S.S. Sun, "Recent progress in organic sensitizers for dye-sensitized solar cells," *RSC Advances*, vol. 5, pp. 23810-23825, 2015.

[5] A. Hagfeldt, G. Boschloo, L. Sun, L. Kloo, and H. Pettersson, "Dye-Sensitized Solar Cells," *Chemical Reviews*, vol. 110, pp. 6595-6663, 2010.

[6] F. Gao, Y. Wang, D. Shi, J. Zhang, M. Wang, X. Jing, "Enhance the Optical Absorptivity of Nanocrystalline TiO2 Film with High Molar Extinction Coefficient Ruthenium Sensitizers for High Performance Dye-Sensitized Solar Cells," *Journal of the American Chemical Society*, vol. 130, pp. 10720-10728, 2008.

[7] R. E. Yasbin, C. R. Matthews, and M. J. Clarke, "Mutagenic and toxic effects of ruthenium," *Chemico-Biological Interactions*, vol. 31, pp. 355-365, 1980.

[8] G. Calogero, G. Di Marco, S. Cazzanti, S. Caramori, R. Argazzi, A. Di Carlo, "Efficient dye-sensitized solar cells using red turnip and purple wild sicilian prickly pear fruits," *International journal of molecular sciences*, vol. 11, pp. 254-267, 2010.

[9] W. Ghann, H. Kang, T. Sheikh, S. Yadav, T. Chavez-Gil, F. Nesbitt., "Fabrication, Optimization and Characterization of Natural Dye Sensitized Solar Cell," *Scientific Reports*, vol. 7, p. 41470, 2017.

[10] N. T. R. N. Kumara, A. Lim, C. M. Lim, M. I. Petra, and P. Ekanayake, "Recent progress and utilization of natural pigments in dye sensitized solar cells: A review," *Renewable and Sustainable Energy Reviews*, vol. 78, pp. 301-31, 2017.

[11] K. Cvetanovic Zobenica, U. Lacnjevac, M. Etinski, D. Vasiljevic-Radovic, and D. Stanisavljev, "Influence of the electron donor properties of hypericin on its sensitizing ability in DSSCs," *Photochemical & Photobiological Sciences*, vol. 18, pp. 2023-2030, 2019.

[12] G. M. Calixto, J. Bernegossi, L. M. de Freitas, C. R. Fontana, and M. Chorilli, "Nanotechnology-Based Drug Delivery Systems for Photodynamic Therapy of Cancer: A Review," *Molecules*, vol. 21, p. 342, 2016.

[13] J.-Y. Liao, J.-W. He, H. Xu, D.-B. Kuang, and C.-Y. Su, "Effect of TiO2 morphology on photovoltaic performance of dye-sensitized solar cells: nanoparticles, nanofibers, hierarchical spheres and ellipsoid spheres," *Journal of Materials Chemistry*, vol. 22, pp. 7910-7918, 2012.

[14] N. Tasić, Z. Marinković Stanojević, Z. Branković, U. Lačnjevac, V. Ribić, M. Žunić, "Mesoporous films prepared from synthesized TiO2 nanoparticles and their application in dye-sensitized solar cells (DSSCs)," *Electrochimica Acta*, vol. 210, pp. 606-614, 2016.

[15] S. P. R. Petrović, Ljiljana; Grbić, Boško; Radić, Nenad; Dostanić, Jasmina; Stojadinović, Stevan; Vasilic, Rastko, "Morphology and fractal dimension of TiO 2 thin films," *Macedonian Journal of Chemistry and Chemical Engineering*, vol. 32, p. 9, 2013.

[16] Y.-F. Chen, C.-Y. Lee, M.-Y. Yeng, and H.-T. Chiu, "The effect of calcination temperature on the crystallinity of nanopowders, "*Journal of Crystal Growth*", col 247, pp. 363-370, 2003.

[17] S. Ito, P. Chen, P. Comte, M. K. Nazeeruddin, P. Liska, P. Péchy, *et al.*, "Fabrication of screen-printing pastes from TiO2 powders or dye-sensitised solar cells," *Progress in Photovoltaics: Research and Applications*, vol. 15, pp. 603-612, 2007.

An Overview of Applications and Integrated Circuit Design Techniques for Semiconductor Gas Sensors

Vladimir M. Milovanović, *Senior Member, IEEE*

***Abstract*—A gas sensor as the device that detects the presence and quantitatively measures the concentration of the certain gas analyte is in pervasive use even nowadays. Nevertheless, with further technological advancement which will imply smaller form factors, lower power consumption and reduced unit prices, this sensor type is expected to become ubiquitous in the Internet of Things era. Semiconducting metal oxides are currently considered as the most promising sensing material to fulfill the foreseen agenda of gas sensor omnipresence. One of the major factors is the processing compatibility with CMOS fabrication technology which allows sensor conditioning and interface circuitry to be cointegrated onto the same chip. This paper gives a brief snippet of some semiconductor gas sensor applications which range from industrial safety and security, over use in health care and medical, all the way up to air quality and environmental monitoring, and automotive. An overview of the MOx gas sensor support circuits with an accent on integrated implementations is also scratched.**

***Index Terms*—Gas sensors, applications, signal conditioning, interface circuitry, chemiresistor, semiconducting metal oxides.**

I. Introduction

Our society is in the midst of the so-called sensor revolution: the Internet of Things (IoT), comprising smart appliances and smart gadgets, as well as ever more powerful wearable and mobile consumer devices fuel the demand for smarter sensor solutions. Applications of gas sensors which provide information about the presence and concentration of a particular gas or gases are virtually countless. These gas sensors not only have the potential to improve the service quality in numerous existing fields, but are also anticipated to be the driving force for many novel use-cases in the near and foreseeable future.

Historically, gas sensors were built as discrete components and reserved for relatively low-volume markets. However, a prospective single-chip integrated solution with a low unit cost, slight power consumption and small form factor would lead to their omnipresence in consumer and industrial electronic devices, along with probable pervasive use in a variety of areas spanning from agriculture to automotive and from environmental to healthcare. This will probably occur in the next decade when certain types of gas sensors are expected to become just as common as humidity or temperature sensors are today.

Miniaturization of gas sensors drives the development of electronic noses in miscellaneous fields. Such noses contain an array of dozen or more sensors, which dominantly exploit gas sensors based on chemiresistive semiconducting metal oxides.

This manuscript is organized as follows: Section II elaborates on contemporary semiconductor gas sensor applications, while the following Section III gives an elementary overview of the support circuits. Finally, Section IV concludes the paper.

V. M. Milovanović is with the Faculty of Engineering, University of Kragujevac, Sestre Janjić 6, 34000 Kragujevac, Serbia (e-mail: vlada@kg.ac.rs).

II. Applications of Semiconductor Gas Sensors

The current global gas sensor market size has been roughly estimated [1], [2] to be worth somewhere in-between one and two billion euros and is anticipated to have the annual growth rate of about 5-10% in the forthcoming decade. This effective market doubling in the next ten years is partially going to be driven by regulatory initiatives in developed markets which will lead to increased demand for smart and wireless gas sensors. The major factors driving the growth besides increasing enforcement of health and safety regulations by governments and continuous development of ever cheaper and miniaturized gas sensors, is also the raised awareness of indoor and outdoor air quality control among general population.

The single most significant obstacle on the road toward more widespread use of gas sensors is their price. Cost of the majority of gas sensors on the market today is in a range of a dozen of euros. However, almost exclusively, these sensors, which are discrete components, are embedded in instruments that bring the price up to and excess of hundreds or even thousands of euros. This greatly limits their application areas.

The future gas sensor market expansion is also likely going to come through unit cost reduction which will be achieved by further sensor miniaturization and co-integration with signal drive and conditioning, as well as processing circuitry. Such solid-state gas sensors [3] integrated alongside standard low-cost manufacturing technology (like CMOS process for example) flow with price tags which will be as low as couple of euros per piece including read-out interfaces [4] would open several high-volume markets. Namely, towards the end of the next decade, gas sensors could potentially be included into many consumer electronic products such as laptops, tablets, cell phones and even smart watches. In this aspect they could follow related success stories of low-cost temperature, barometric pressure and/or humidity sensors which all incorporate the sensing element together with surrounding electronics.

Certainly, cost factor is not the only impediment to making a commercially successful sensor. Sensor characteristics are generally summarized through its "4S": **s**ensitivity, **s**electivity, **s**tability and **s**peed of response and recovery. Besides these metrics, also of paramount importance is sensor size and power consumption, especially in mobile or wireless sensor network battery-powered applications, and other mass markets like the Internet of Things (IoT) or wearables. The last requirement is particularly challenging when one considers that for optimum performance the majority of gas sensors must be heated by a separate heating element to operating temperatures which are well-above the ambient. Notwithstanding, the intermittent gas sensor operation is the usual method to relax this concern.

Nowadays, semiconductor gas sensors are applied and find their use cases in a wide variety of fields. As an illustrative starting example, at the beginning of the periodic table of elements sits hydrogen with the atomic number 1. It is the lightest of all elements and, since on standard pressures and temperatures hydrogen with molecular formula H_2 is a colorless, odorless and tasteless, it cannot be detected by human senses. Moreover it is highly combustible and flammable gas. With air the hydrogen forms explosive mixture which may be ignited in a spontaneous reaction. On the other hand hydrogen finds its direct end use cases as fuel and propellant in hydrogen powered vehicles and aerospace operations, respectively. Indirectly hydrogen observation is important in plethora of spheres ranging from everyday ones like detection of environmental pollution or indication of certain diseases up to an early sign of fire or reactors safety inside nuclear power plants. Hydrogen presence detection and concentration quantification also finds its applications in semiconductor manufacturing and revealing of impending transformer failure in electric power plants.

Therefore the detection of hydrogen leaks and measurement of its concentration is essential from production and storage, to transportation and use in both mobile and stationary applications. Hydrogen gas sensors [5] are hence necessary in each sector of the emerging hydrogen economy, in which hydrogen gas is exploited as an energy carrier and as a chemical reactant, as they monitor safety in production plants, storage tanks, refueling stations and combustors and engines themselves.

Totally different, but equally illustrative example are the so-called volatile organic compounds (VOCs), which are basically high vapor pressure organic chemicals. VOCs are both numerous and ubiquitous, and while some of them can cause harm to human health, others present a danger to the environment.

Typically harmful VOCs are not acutely toxic, but if generated inside houses may cause sick building syndrome. Some of them can have compounding long-term health effects and are even carcinogenic. On the other hand, VOCs can also be found inside the human body. Particularly, a breath contains thousands of VOCs which can either originate from within the body (endogenous VOCs) or from external sources such as diet, prescription drugs or environmental exposure (exogenous VOCs). More details on the breath biopsy will be given later, but semiconductor gas sensors that can detect total VOC (TVOC) concentrations indoor, or specific compounds during breath screening are fundamental component in both scenarios.

Apart from single dedicated gas sensors there is an increasing desire to simultaneously measure more than one gas. In other words, there exists a growing demand to have multi-gas sensing systems with roughly speaking a dozen of sensors (which may also include ambient temperature, humidity and barometric pressure). Such an array in which every individual sensor is not specific to a particular gas, but rather has different sensing pattern, is the basis for the fundamental sensing system commonly known as “electronic nose”. In combination with a pattern recognition module, the e-nose [6] is considered to be a genuine artificial olfaction structure for odor characterization.

Both, individual gas sensors and gas sensor arrays, nowadays are in pervasive use in a variety of spheres. An outlook of some application areas is given in the following subsections.

A. Safety and Security

A snippet of applications of hydrogen gas sensors was given above. As seen, their main purpose is safety in various places. Hydrogen is not an exception here. There are other examples of hazardous and toxic gases that should be kept under control. As is well-known the demand and application of gas sensors in practice began with the inflammable gas alarms [7] to protect people from fatal gas hazards such as exposure to poisonous gases and gas explosions or incomplete combustion accidents. Fire alarms usually combine smoke and/or thermal detector together with a semiconductor gas sensor and are literaly found in every place where humans live, from residential buildings and hotels to schools and office space. Gas sensors are found in homes for, e.g., monitoring flammable gas level inside gas-fired boilers. There has also been an increasing demand for workplace safety in coal mines or certain industries like petrochemical, to name a few. Actually, the success story of semiconductor gas sensors can be partially explained by their high sensitivity to a broad range of inflammable and toxic gas species and their simple detection principle relying on changes of electrical conductance due to interaction with the gas.

Historically, this was actually the first use case of gas sensors that exploit semiconducting metal oxides. The pioneering work of Naoyoshi Taguchi in Japan led to electrochemical gas sensor discovery being the first commercial device [8] that was used to detect low concentrations of combustible and reducing gases. Later he founded the company Figaro Engineering Inc., which is still today the largest manufacturer of semiconductor gas sensors worldwide. The original Taguchi gas sensor (TGS) is a highly-sensitive device, rather than highly-stable, making it ideal for gas alarms and economical detection of potentially explosive concentrations of inflammable gases in general.

Even though traditionally, single gas sensor was responsible for a particular safety monitoring purpose, integrating multiple gas sensors is gaining popularity with the increased availability of affordable sensors. For example in a boiler combustion process, there is a requirement to measure hydrogen or methane, as well as carbon oxides (monoxide/dioxide) and even oxygen.

Semiconducting metal oxide gas sensors can be employed to construct multi-sensor units (marketed as FireNose) that are utilized to discover and discriminate between known and unknown gases in harsh and uncontrolled conditions [9] or mobile (rescue) robots for gas leak detection and localization [10], as well as toxic smoke real-time mapping which could serve as an aid to firefighter brigades and teams. The field of mobile robotic olfaction customarily considers gas source localization and gas distribution mapping as two of its main tasks.

Oxygen sensors are indispensable in non-air breathing gas scuba diving or other hyperbaric use cases. In every such scenario, it is essential that the constituents of the breathing gas mixture are precisely kept at the correct concentrations.

Finally, a breathalyzer (a portmanteau of breath and analyzer), i.e., a portable handheld breath alcohol checker that detect ethanol vapour in human breath for preventing drunken driving are also examples of semiconductor gas sensors used for safety purposes. Interestingly, the very same semiconductor gas sensors are not only exploited inside car ignition locking system but are also utilized inside a brewing process control.

B. Health Care and Medical

While some gases are toxic and hazardous, others may be vital for life and symptomatic of health conditions. Perhaps the most dominant gas sensor overall by gas type is the oxygen one. Besides industrial applications where it is widely used in automotive, building automation for smart cities and food and beverages, it is beyond doubt the leader in health and medical equipment. In this area, the oxygen sensors are used in incubators and other hypoxic life science products, like patient and breathe monitoring systems, anesthesia monitors, lung function diagnosis systems, respirators/ventilators, and oxygen concentrators. Besides oxygen, other anesthetic and respiratory gases are regularly monitored during operations.

Detection of disease-related gases is drawing increasing attention for medical purposes. Exhaled human breath contains thousands of different volatile organic compounds (VOCs) which are usually measured in the sub-ppm level or even lower concentrations for healthy subjects. The attractiveness of VOC analysis comes from its absolutely non-invasive character and can be applied to any stage of life from early childhood to late adulthood. Even though the correlation between certain disease and some VOCs was well known for more than a century, only modern instruments based on semiconductor gas sensors can give quantitative measures necessary for strict clinical practice. Independent clinical trials [11] have shown the possibility of using breath for detecting serious illnesses, such as different types of cancer, diabetes, Alzheimer's and Parkinson's disease, multiple sclerosis, tuberculosis, chronic kidney disease, among other. An additional burst to the interest in VOCs examination and analysis for medical purposes has been provided by the development and the diffusion of solid-state gas sensors [12], therefore in the foreseeable future breath tests are expected to become just as common (if not more) as blood tests are today.

Specific breath biomarkers can not only indicate a presence of some diseases, but can also reflect general physical condition. An example of such devices are portable acetone analyzers that measure the ketone level and calculate body fat burning rate just from exhaled breath. These pocket-sized accessories that monitor fat metabolism and levels of ketosis are in a widespread use in various diet and fitness programs.

Besides being applied in healthcare, gas sensors are, along the similar path, also more and more part of the fast developing wearable biosensors market. These wearable biosensors [13] are complex miniature devices that incorporate wireless communication modules for transmitting sensor data to computing infrastructure. A variety of substances are used in such sensing devices. As an illustration, for semiconducting oxide materials this is a real challenge as it is necessary to reduce the sensor operating conditions to room temperature. One way to achieve this is through nanostructures, like graphene [14] or nanowires. Recently, even flexible and stretchable self-heating metal oxide (MOx) gas sensing platform [15] has been demonstrated.

Compared to their industrial counterparts, the development of wearable gas sensors needs to address additional challenging requirements, including lightweight and small form factor, low operating temperature, low energy consumption, and mechanical robustness upon various skin deformations.

C. Air Quality and Environmental Monitoring

Pollution and urban air quality are the major environmental risks [16] to public health. Gas emissions are responsible for a variety of respiratory illnesses and environmental problems, such as acid rain and the depletion of the ozone layer. Pollutants may be released from natural sources and they can be man-made or anthropogenic. Natural sources of air pollutants are lightning, soils, fires and volcanoes while anthropogenic sources incorporate emissions from human activity — for example, exhaust gases from transportation, chemical accidents or industrial actions such as power plants and landfill sites.

Many countries express air quality in terms of the air quality index which is calculated based on concentrations of several key air pollutants [17] such as ground-level ozone, particulates, sulfur dioxide, carbon monoxide and nitrogen dioxide.

Some of these are powerful oxidizing toxic gases that have noxious effects on both vegetation and human health. Ozone, as a secondary pollutant, for example, has become of growing importance in ambient air during the last decades [18] and has been identified as the main agent responsible of heavy peaks of pollution in urban atmospheres during warm sunny periods.

Commonly, data on air quality are collected from monitoring stations, which contain a sensor for each pollutant or a gas sensor array [19], just like in electronic nose. Currently, many monitoring systems consist of a static network of air quality sensors that are distributed at key locations and can produce a spatially-resolved picture of pollution variations on the urban scale. Consequently, in order to obtain a truthful representation of the gas distribution and be able to locate gas sources, it is essential to collect spatially distributed gas concentration data.

Mobile robots equipped with gas detectors were also used in outdoor applications for pollution monitoring and source localization in public areas, surveillance of industrial facilities producing harmful gases, and monitoring of landfill sites. Portable electronic nose featuring on-demand operation [20] is particularly neat for the IoT and wireless sensor networks.

More recently, gas monitoring outdoors was also addressed using unmanned aerial vehicles (UAVs), commonly known as drones, although with far more power and size constraint [21] limitations placed upon gas sensors. In addition to air quality and environmental monitoring in general [22], an individual and a swarm of micro and nano drones [23] have also been employed for volcanic gas sampling, localization of fugitive emissions, early fire detection, precision agriculture, landfill monitoring and mine blasting, among many other use cases.

The tiny form-factor and maneuverability of UAVs allow sensing of hazardous environments inaccessible to terrestrial robots. Miniaturization of semiconductor gas sensors made possible equipping drones with olfaction capabilities which can be exploited in myriad of applications. For example, in the aftermath of an earthquake or explosion drones could navigate such scenarios much faster and sample the space in 3D.

Both indoor and outdoor air quality concerns are driving the applications not only in environmental monitoring but in commercial building automation too. Therefore, gas sensors are experiencing a high demand in Heating, Ventilation and Air Conditioning (HVAC) control systems as they facilitate intelligent ventilation control based on gas concentrations.

Furthermore, air quality sensors are usually incorporated into air cleaners, deodorizers, ionizers, purifiers and air sanitizers for energy saving purposes or just plain amenity also.

D. Automotive

Modern cars include abundance of gas sensors located both inside and outside of cabin which serve either as a commodity or an essential indispensable part in the engine compartment.

It is nowadays fairly common to have the electronic control unit (ECU) of a car to automatically close and open the fresh air flaps [24], depending on the ambient gas concentration measured in the air-intake manifold under the hood of the car. Typical gases that are monitored are combustion-related compounds. Therefore, a pair of CO and NO_2 sensitive sensors are regularly installed into a damper system to determine the "outside air quality level". In addition, car interior could also exhibit multiple sources of disturbing gases like cigarette smoke, food odor, or bioeffluents, which are detected by sensor system directly mounted within the cabin of a passenger vehicle to define the "inside air quality level" thus requiring more sophisticated air and climate-management concepts. This means that based on interior and exterior semiconductor gas sensor readings contemporary automotive heating, ventilation, and air conditioning (HVAC) systems can decide to take no action, close the recirculation flap in case of bad outside air quality level, increase air exchange rate in case of bad inside air quality level, or start active air cleaning in addition to the flap closure in case of bad inside and outside air quality levels.

Besides external and internal air quality level monitoring, just as important are oxygen sensors, for this particular application more frequently referred to as the lambda sensor, where lambda (λ) refers to air–fuel equivalence ratio, which measure the exhaust-gas concentration of oxygen for internal combustion engines in order to calculate and dynamically adjust the air-fuel ratio so that catalytic converters can perform properly and work optimally. The lambda sensors, which are in modern cars more and more semiconductor based, make today's electronic fuel injection and emission control possible.

E. Industrial

Applications of semiconductor gas sensors in industry are virtually countless and span across every industrial branch.

Mining and in particular, the underground mining exposes workers to flammable gas, asphyxiants, oxygen depletion and a range of toxic gas hazards. To keep miners safe, both fixed and portable detectors are deployed to ensure that if a dangerous condition arises, audible and visual alarms are generated so that evacuation can occur rapidly. Likewise, in gas and oil industry, whether upstream in the production process (exploration and extraction) or downstream (transportation, processing, storage) or around the distribution pipelines, many different gas detectors are used for process control as well as for staff and plant protection against explosion or the presence of toxic gases. Gas sensors are also used at rig and processing locations to monitor the concentration of the gases released into the Earth's atmosphere. Similar use cases of gas sensors for various process control and safety of the employed personnel are encountered in petrochemical industry too.

Apart from toxic and explosive gas detection for the purpose of domestic, industrial and public safety, semiconductor gas sensors are used in beverage and food industries to control the fermentation processes. A very interesting application is in intelligent food packaging [25] used to detect rotten or spoiled food using cheap gas sensors. For instance, these sensors can identify spoilage gases like ammonia in meat and fish products and can be read by smartphones. Even though the concept of food quality control [26] using gas sensors is already known for quarter of a century, it became economically feasible only recently. Eventually, these low-cost gas detectors with prices in the order of one cent might eventually replace the "use-by" date stickers, as much more reliable freshness indicator. As a consequence these sensors could partially reduce food waste, but more importantly cut the yearly number of food poisoning.

More advanced multisensor arrays inside an electronic nose have been applied to determine optimal beef aging time [27] and monitor meat quality as well as to control food in general.

F. Electronic nose (e-nose or eNose)

A contemporary electronic nose system typically consists of a multisensor array, an information-processing unit such as an artificial neural network, software with digital pattern-recognition algorithms, and reference-library database of digital aroma fingerprint signatures. These systems have been designed specifically to be used in numerous application areas.

Even though different types of gas sensor are employed in e-nose systems, semiconductor-based gas sensors are preferred primarily thanks to their fast response and recovery times [28], but also because their small size, low manufacturing cost and acceptable power consumption [29] even for handheld devices.

Example use cases of electronic noses [30] practically do correspond to those of gas sensors themselves and include (in no particular order): explosive and flammable material detection for public safety and welfare as well as for passenger and personnel security in airline transportation; perfume and cologne development and choice of fragrance additives as well as personal application product enhancement and consumer appeal in cosmetics; ingredient or product consistency confirmation for brand recognition and consumer fraud prevention as well as detecting off-flavors and characterizing taste and smell to determine contamination or ripeness or spoilage inside food and beverage quality control assessment; safe food supply and corp protection, corp ripeness and preservation treatments for harvest timing and storage inside agriculture; checking product characteristics and consistency for processing controls as well as aroma and flavor uniformity across products, but also toxic gas leak detection and fire alarms for the purposes of safety, security and proper work conditions inside any manufacturing industrial sector; pathogen identification and disease detection together with patient treatment selection and prognoses as well as checking nutrition status, organ failures, disease diagnoses, metabolic disorders and general physiological conditions inside medical, healthcare and clinical sectors; biological and chemical weapons and explosive materials detection in defense and military sectors; quality control of drug purity including formulation consistency and uniformity in product mixtures for pharmaceutical industry; among many other example cases.

III. Gas Sensor Signal Conditioning & Interfaces

Mainly, semiconductor gas sensor interface circuitry depends whether hybrid or monolithic approach has been used.

1) Hybrid: Traditionally, integration is realized with the so-called multi-chip approach in which the sensor and circuits are designed and fabricated on separate chips. There are multiple advantages of this two-chip solution. First, this implementation scenario enables independent adjustment and optimization of the gas sensor and the interface circuitry thus providing much more flexibility in the design and fabrication which leads to shorter development cycles. Furthermore, if there is a problem with the sensing device, the same circuitry can be reused, thus enhancing manufacturing yield. However, extra cost is incurred by the complex packaging. Also, parasitic capacitances and inductances associated with long bonding wires and interconnect are undesirable and can give rise to increased noise and signal degradation. Additionally, the hybrid approach is less robust and more expensive with respect to single-chip implementation particularly when considering high volume production.

2) Monolithic: A more recent and a more advanced method is the so-called monolithic approach in which both the sensor and circuitry are designed and fabricated on the same substrate. This single-chip solution enhances the gas sensor performance by reducing its overall size, power consumption and noise. It is also more cost-efficient and hence more commercially attractive in high unit volumes. The additional challenges arise from limitation of process compatible gas sensor materials and prolonged and costly development cycle. Also, a potential fault in either a sensor or the nearby circuitry will result in the complete chip failure. Thermal isolation is crucial since the main challenge is that the operating temperature of the metal oxides exceeds maximum operating temperature of the CMOS-based silicon integrated circuits. But, if a proper isolation mechanism is employed [31], only several degrees difference between the sensor circuit and the ambient temperature can be achieved.

The main operating principles of chemiresistive gas sensors, including there semiconducting metal oxide sensors, is based on the change of conductivity/resistivity of the oxide on interaction with a gas and this dependence is usually proportional to the concentration of the gas. By the rule, the gas sensor itself has a bell-shaped temperature dependent response with a maximum at elevated temperatures. Therefore, semiconductor gas sensors also incorporate integrated (micro)heaters as well.

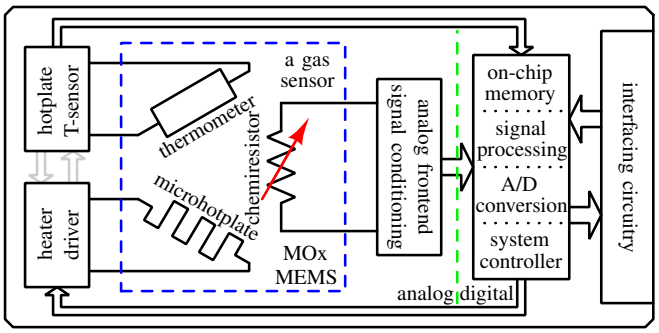

Fig. 1. A chemiresistive MOx gas sensor model and the surrounding circuitry.

A. Heater Driving and Sensing Circuitry and the Controller

Since the gas sensor response greatly depends on the precise temperature, the heater driving and temperature control makes a crucial part of the overall gas sensor system. The temperature control circuitry becomes more challenging when it is taken into account that semiconductor metal oxide sensors can be operated either in isothermal (that is, constant temperature) or temperature-modulated regime, the latter being more complex but provides insight into distinguishing temporal response [32] pattern based on which different analytes can be discriminated.

1) Heater Driver: Heaters are driven either by a current or voltage source. Circuits are designed to provide a source either at a static (e.g., DC) or modulated (e.g., AC or pulsed) level. In case of a voltage drive, commonly a bandgap voltage reference and a current limiter are required to provide an accurate and stable voltage and avoid any overheating damage. In case of current drive, a current mirror is employed. In both cases it is desirable to measure the power through the heater and provide an indication [4] of temperature and general operating status.

2) Temperature Sensor: Since the sensing material temperature plays a vital role in improving the selectivity of almost any gas sensor, either a dedicated temperature sensor can be deployed or the change of heater resistance with temperature can be exploited to estimate the actual temperature of the heater itself. Even though separate temperature sensors bring additional circuit complexity & cost, they are often much more reliable approach especially when tied with the pulsed driving.

3) Controller: With the incorporation of a microheater and temperature sensor of some sort, there are several ways how to monitor and control the heater temperature. The heater can be controlled in binary on-off mode (also referred to as the "bang-bang" controller), proportional mode or proportional integral derivative (PID) mode which eliminates the steady-state error while offering rapid response time without overshoot. In case the temperature sensor readings are digitized and compared to a digital preset value, a digital controller can be designed to achieve very accurate and flexible soft-programmable control.

B. Sensing Material Measurement and the Readout Interface

Interfacing circuitry design is one of the most challenging components mainly because it has to: (i) handle the precision and dynamic range of the gas sensing element whose baseline sheet resistance can vary from k$\Omega/\square$ all the way up to G$\Omega/\square$; and (ii) compensate for the drift in the baseline resistance of the sensing material. The simplest scheme involves resistance-to-voltage conversion either through a resistive voltage divider or a Wheatstone bridge. When seeking full integration, these techniques are not ideal as they require either a resistor bank circuit with very large value or a trimming or variable resistors to cover wide range and match the sensing material resistance.

Another approach is to use the resistance-to-frequency conversion instead, but in order to cover a very high dynamic range the parasitic capacitance associated with the sensing material has to be retrieved and isolated [33] to avoid resistance measurement contamination in the high frequency portion.

A relatively simple idea to use a logarithmic converter (utilizing exponential characteristics of a diode) to compress the large dynamic range but it inevitably compromises accuracy.

By the rule, contemporary sensors include the analog front-end circuitry which consists of amplifiers that increase sensor signal fidelity as well as analog-to-digital (A/D) converters.

Digital sensor platforms which are becoming increasingly popular [34] because they effectively co-integrate analog and digital electronics together with a microhotplate and the sensing elements onto a single die. They allow more advanced signal processing circuitry in the digital domain and also incorporate digital interface that greatly simplifies the integration into different applications, since the output signal can be directly used by customers without further processing.

IV. Conclusions

Semiconductor gas sensors, also known as MOS sensors, that are constructed on the basis of a semiconducting metal oxide (MOx), detect gases by a chemical reaction that takes place when the gas comes in direct contact with the sensor.

Over the past several years they became pervading across many industrial sectors. One of the main reasons is cointegration with the nearby circuitry which triggered the constant improvement in performance in combination with ever lower price tags. This trend will most certainly continue in the future.

References

[1] Global Market Insights, Inc. (2018, Nov.) Gas sensors market size, industry analysis report, regional outlook, application potential, price trend, competitive market share & forecast. [Online]. Available: www.gminsights.com/industry-analysis/gas-sensors-market-size

[2] Grand View Research, Inc. (2020, Feb.) Gas sensor market size, share & trends industry analysis report. [Online]. Available: www.grandviewresearch.com/industry-analysis/gas-sensors-market

[3] C. Hagleitner, A. Hierlemann, D. Lange, A. Kummer, N. Kerness, O. Brand, and H. Baltes, "Smart single-chip gas sensor microsystem," *Nature*, vol. 414, no. 6861, pp. 293–296, 2001.

[4] J. W. Gardner, P. K. Guha, F. Udrea, and J. A. Covington, "Cmos interfacing for integrated gas sensors: A review," *IEEE Sensors Journal*, vol. 10, no. 12, pp. 1833–1848, 2010.

[5] T. Hübert, L. Boon-Brett, G. Black, and U. Banach, "Hydrogen sensors – a review," *Sensors and Actuators B: Chemical*, vol. 157, no. 2, pp. 329–352, 2011.

[6] H. T. Nagle, R. Gutierrez-Osuna, and S. S. Schiffman, "The how and why of electronic noses," *IEEE Spectrum*, vol. 35, no. 9, pp. 22–31, 1998.

[7] N. Yamazoe and K. Shimanoe, "Chapter one - fundamentals of semiconductor gas sensors," in *Semiconductor Gas Sensors (Second Edition)*, second edition ed., ser. Woodhead Publishing Series in Electronic and Optical Materials, R. Jaaniso and O. K. Tan, Eds. Woodhead Publishing, 2020, pp. 3–38.

[8] J. Watson and D. Tanner, "Applications of the Taguchi gas sensor to alarms for inflammable gases," *Radio and Electronic Engineer*, vol. 44, no. 2, pp. 85–91, 1974.

[9] Y. Xing, T. A. Vincent, H. Fan, E. Schaffernicht, V. Hernandez Bennetts, A. J. Lilienthal, M. Cole, and J. W. Gardner, "FireNose on mobile robot in harsh environments," *IEEE Sensors Journal*, vol. 19, no. 24, pp. 12 418–12 431, 2019.

[10] J. Palacín, D. Martínez, E. Clotet, T. Pallejà, J. Burgués, J. Fonollosa, A. Pardo, and S. Marco, "Application of an array of metal-oxide semiconductor gas sensors in an assistant personal robot for early gas leak detection," *Sensors*, vol. 19, no. 9, p. 1957, 2019.

[11] G. Konvalina and H. Haick, "Sensors for breath testing: From nanomaterials to comprehensive disease detection," *Accounts of Chemical Research*, vol. 47, no. 1, pp. 66–76, 2014.

[12] C. Di Natale, R. Paolesse, E. Martinelli, and R. Capuano, "Solid-state gas sensors for breath analysis: A review," *Analytica Chimica Acta*, vol. 824, pp. 1–17, 2014.

[13] S. Khan, S. Ali, and A. Bermak, "Recent developments in printing flexible and wearable sensing electronics for healthcare applications," *Sensors*, vol. 19, no. 5, p. 1230, 2019.

[14] M.-A. Kang, S. Ji, S. Kim, C.-Y. Park, S. Myung, W. Song, S. S. Lee, J. Lim, and K.-S. An, "Highly sensitive and wearable gas sensors consisting of chemically functionalized graphene oxide assembled on cotton yarn," *RSC Adv.*, vol. 8, pp. 11 991–11 996, 2018.

[15] L. Yang, N. Yi, J. Zhu, Z. Cheng, X. Yin, X. Zhang, H. Zhu, and H. Cheng, "Novel gas sensing platform based on a stretchable laser-induced graphene pattern with self-heating capabilities," *J. Mater. Chem. A*, vol. 8, pp. 6487–6500, 2020.

[16] R. Binions and A. J. T. Naik, "Chapter thirteen - metal oxide semiconductor gas sensors in environmental monitoring," in *Semiconductor Gas Sensors (First Edition)*, ser. Woodhead Publishing Series in Electronic and Optical Materials, R. Jaaniso and O. K. Tan, Eds. Woodhead Publishing, 2013, pp. 433–466.

[17] P. J. D. Peterson, A. Aujla, K. H. Grant, A. G. Brundle, M. R. Thompson, J. Vande Hey, and R. J. Leigh, "Practical use of metal oxide semiconductor gas sensors for measuring nitrogen dioxide and ozone in urban environments," *Sensors*, vol. 17, no. 7, p. 1653, 2017.

[18] L. Talazac, F. Barbarin, L. Mazet, and C. Varenne, "Improvement in sensitivity and selectivity of InP-based gas sensors: pseudo-Schottky diodes with palladium metallizations," *IEEE Sensors Journal*, vol. 4, no. 1, pp. 45–51, 2004.

[19] C. S. Prajapati, R. Soman, S. B. Rudraswamy, M. Nayak, and N. Bhat, "Single chip gas sensor array for air quality monitoring," *Journal of Microelectromechanical Systems*, vol. 26, no. 2, pp. 433–439, 2017.

[20] C. J. García-Orellana, M. Macías-Macías, H. M. González-Velasco, A. García-Manso, and R. Gallardo-Caballero, "Low-power and low-cost environmental IoT electronic nose using initial action period measurements," *Sensors*, vol. 19, no. 14, p. 3183, 2019.

[21] M. Rossi and D. Brunelli, "Autonomous gas detection and mapping with unmanned aerial vehicles," *IEEE Transactions on Instrumentation and Measurement*, vol. 65, no. 4, pp. 765–775, 2016.

[22] T. F. Villa, F. Gonzalez, B. Miljević, Z. D. Ristovski, and L. Morawska, "An overview of small unmanned aerial vehicles for air quality measurements: Present applications and future prospectives," *Sensors*, vol. 16, no. 7, p. 1072, 2016.

[23] J. Burgués, V. Hernández, A. J. Lilienthal, and S. Marco, "Smelling nano aerial vehicle for gas source localization and mapping," *Sensors*, vol. 19, no. 3, p. 478, 2019.

[24] M. Blaschke, T. Tille, P. Robertson, S. Mair, U. Weimar, and H. Ulmer, "MEMS gas-sensor array for monitoring the perceived car-cabin air quality," *IEEE Sensors Journal*, vol. 6, no. 5, pp. 1298–1308, 2006.

[25] S. Matindoust, M. Baghaei-Nejad, M. Shahrokh Abadi, Z. Zou, and L.-R. Zheng, "Food quality and safety monitoring using gas sensor array in intelligent packaging," *Sensor Review*, vol. 36, no. 2, pp. 169–183, 2016.

[26] N. Funazaki, A. Hemmi, S. Ito, Y. Asano, Y. Yano, N. Miura, and N. Yamazoe, "Application of semiconductor gas sensor to quality control of meat freshness in food industry," *Sensors and Actuators B: Chemical*, vol. 25, no. 1, pp. 797–800, 1995.

[27] M. Ghasemi-Varnamkhasti, S. S. Mohtasebi, M. Siadat, and S. Balasubramanian, "Meat quality assessment by electronic nose (machine olfaction technology)," *Sensors*, vol. 9, no. 8, pp. 6058–6083, 2009.

[28] K. Arshak, E. Moore, G. M. Lyons, J. Harris, and S. Clifford, "A review of gas sensors employed in electronic nose applications," *Sensor Review*, vol. 24, no. 2, pp. 181–198, 2004.

[29] A. Dey, "Semiconductor metal oxide gas sensors: A review," *Materials Science and Engineering: B*, vol. 229, pp. 206–217, 2018.

[30] A. D. Wilson and M. Baietto, "Applications and advances in electronic-nose technologies," *Sensors*, vol. 9, no. 7, pp. 5099–5148, 2009.

[31] H. Liu, L. Zhang, K. H. H. Li, and O. K. Tan, "Microhotplates for metal oxide semiconductor gas sensor applications—towards the CMOS-MEMS monolithic approach," *Micromachines*, vol. 9, no. 11, p. 557, 2018.

[32] A. P. Lee and B. J. Reedy, "Temperature modulation in semiconductor gas sensing," *Sensors and Actuators B: Chemical*, vol. 60, no. 1, pp. 35–42, 1999.

[33] P. K. Guha, S. Santra, and J. W. Gardner, "Chapter fourteen - integrated CMOS-based sensors for gas and odor detection," in *Semiconductor Gas Sensors (Second Edition)*, second edition ed., ser. Woodhead Publishing Series in Electronic and Optical Materials, R. Jaaniso and O. K. Tan, Eds. Woodhead Publishing, 2020, pp. 465–487.

[34] D. Briand and J. Courbat, "Chapter thirteen - micromachined semiconductor gas sensors," in *Semiconductor Gas Sensors (Second Edition)*, second edition ed., ser. Woodhead Publishing Series in Electronic and Optical Materials, R. Jaaniso and O. K. Tan, Eds. Woodhead Publishing, 2020, pp. 413–464.

Influence of vacuum degassing on microchannel plate performance

A. Stanković, I. Zlatković, R. Nikolov, B. Brindić and D. Pantić

***Abstract*— This article discusses the influence of vacuum degassing on the microchannel plate (MCP) performance. Vacuum baking is a process of degassing by heating components to make them release molecules attached to their surfaces (mainly H_2O). Experiments were done with the MCPs with a channel diameter of 6μm, that were backed for 12h at the temperature of 430°C under a high vacuum. The results showed a change in electrical parameters of MCP- the resistance and the gain changed up to 30% and 50%, respectively.**

***Index Terms*—vacuum degassing, vacuum baking, image intensifier tube, microchannel plate, gain, resistance.**

I. Introduction

Microchannel plate as an amplifier is commonly used in various detectors and night vision devices because of its excellent performance in electron multiplication with high gain, high resolution, low noise, and other characteristics [1-4]. Here will be considered the use of MCP in image intensifier tubes (IIT) for night vision devices. IIT is a device that amplifies low light level images to a level that can be seen with the human eye. The key component of IIT is MCP along with photocathode and phosphor screen (Fig.1).

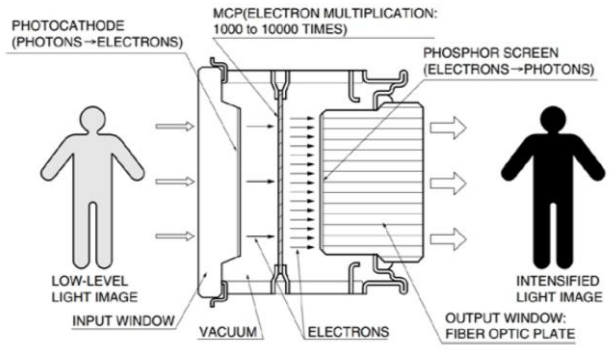

Fig. 1. Image intensifier tube operating principle [3].

A. Stanković, I. Zlatković, and D. Pantić are with the Department of Microelectronics, Faculty of Electronic Engineering, University of Niš, Aleksandra Medvedeva 14, 18000 Niš, Serbia,
E-mail: aleksandra.stankovic@elfak.rs, ivanzlatkovic90@hotmail.com, dragan.pantić@elfak.ni.ac.rs.
R. Nikolov is with Photon Optronics, Bulevar Svetog Cara Konstantina 80-82, 18000 Niš, Serbia, E-mail: rade.nikolov@photonoptronics.rs
Branislav Brindić is with Sova HD, Bulevar Svetog Cara Konstantina 80-82, 18000 Niš, Serbia.

A photocathode as an input window of the image intensifier tube converts incident light (photons) into electrons. Multialkali photocathode is usually used for 2nd generation of image intensifier tubs, or GaAs for 3rd generation image intensifier tubes. Once released by the photocathode these electrons are accelerated and strike the inner wall of MCP channels, where they are amplified. For each electron that enters MCP, approximately one thousand electrons are generated and accelerated from the output of MCP to the phosphor screen, which converts the electrons back into photons.

A. MCP Operating Background

Microchannel plate consists of several million microchannels that are fused and each one serves as an independent electron multiplier. The operating principle of the MCP is based on secondary electron emission (Fig. 1): When an electron enters a channel from the input side it hits the channel's inner wall. In each collision, the electron from the channel wall excites the new 3-8 electrons, which further move accelerated by the influence of a strong electric field developed by a voltage applied across both ends of the MCP, striking the channel wall and exciting new electrons, eventually causing the avalanche of secondary electrons at the output side. This phenomenon of multiplication of an electron under the action of an electric field is called the secondary electron emission. In this way the input signal is increased about 10^3-10^4 times, depending on the operating mode of the MCP and applied voltage.

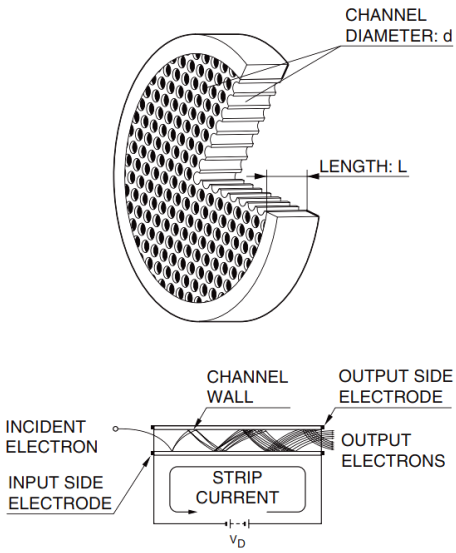

Fig. 2. The structure and operating principle of the MCP [4].

II. VACUUM DEGASSING

The microchannel plate is produced from lead-silicate glass riched in alkalies that can improve the electrical property of the glass. MCP starts as a glass tube (also called cladding) fitted with rode or a core (a soluble glass) and drawn into single-fiber, then a number of these single-fibers are stacked in a hexagonal array called a multi. The entire assembly is drawn again to form multi-fibers. The multi-fibers are then stacked to form a boule which is fused at high temperature. Then sliced on a wafer at a certain angle, polished and then each wafer is chemically processed to remove the core, leaving a honeycomb structure of million microchannels. The next process is hydrogen reduction where the wafer gets its conducting and secondary emissive properties. It is well known that when silica glass with a high amount of lead oxide is treated in hydrogen reduction at elevated temperatures, a semiconductor surface layer is formed. The surface layer of the glass appears black due to formed dispersion lead particles during the chemical reduction of PbO in hydrogen. [5]

After reduction two layers are formed (Fig.3):

- Emission layer 20 nm thick, rich in silica and alkali metals. This layer contains electrons that participate in the secondary emission and determines the gain of the microchannel plate.
- Conductive (resistant) layer 50-100nm thick. This layer is placed deeper in the channel and it is rich in lead. The conductive layer determines another electrical characteristic of MCP and that is its resistance. At the beginning of the reduction process, small lead grains are formed, then at the temperature of 450-500ºC, grains begin grouping into clusters and the principle of conducting the current is the principle of skipping the electron from the clusters to the next clusters of lead. The function of the conductive layer is to donate the electrons to the emission layer for the secondary emission by the support of the strip current. When the electron leaves the lattice of potassium silicate, a hollow left in the lattice is occupied with an electron from a conductive, lead layer and that makes the MCP current ("strip current").

$$R = Umcp / Istrip \quad (1)$$

After hydrogen reduction, some alkaline impurities appear on the surface of the channels due to the diffusion of alkali cations in the surface through the walls. In contact with water vapor, hydrogen, and silicates on the channel walls they form various compounds that can cause excess gas, Ion feedback, etc.

So, from the MCPs fabricate process comes the residual gas molecules that are mainly hydrogen, water, carbon monoxide, and carbon dioxide. These gases make problems later when MCP is sealed in the image intensifier tube. There are two ways to eliminate these gases: electron scrubbing and high-temperature bake with a high vacuum degassing process.

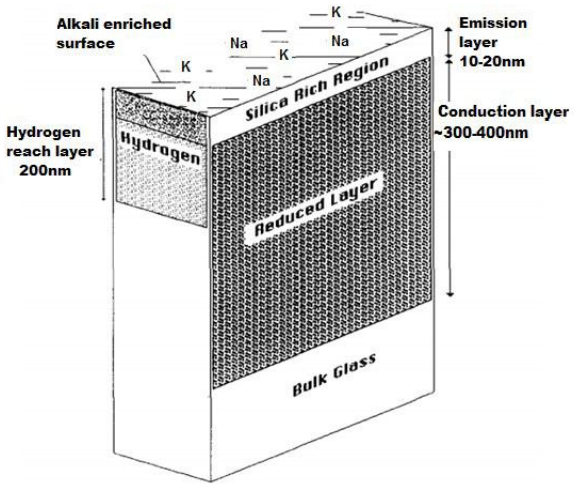

Fig. 3. MCP wall structure [5].

III. RESULTS OF VACUUM DEGASSING

For these experiments, ten MCPs with a channel diameter of 6μm were chosen to see the influence of vacuum degassing on its performances. Before vacuum degassing, all MCPs were tested in a special device for measuring the electrical characteristics of the MCPs, called "Tester". The tester simulates the work of MCP in the image intensifier tube. We can simulate the operation of the MCP in IIT in all modes, from 10^{-5}lux corresponding to total darkness to 10^{2}lux correspondings to daylight. It consists of an ion gun (with tungsten filament), a focusing column, a chamber with an MCP holder, and a phosphorus screen. So resistance and gain at 800V on MCP were measured. After that, the experiment was done under the following conditions: vacuum 10^{-6} mbar, the temperature of 430ºC, and the time of 12h, then tested again. Table 1 shows the changes in MCP gain and the bulk resistance before and after high-temperature vacuum baking.

TABLE I
RESULTS OF THE EXPERIMENT

MCP	Parameters of VD		Results before and after VD					
	T (ºC)	t(h)	R_before [MΩ]	R_after [MΩ]	ΔR (%)	G_before (800V)	G_after (800V)	ΔG(%)
MCP 1	430	12	122.168	159.402	**30.48%**	2378	1164	**-51.05%**
MCP 2	430	12	81.135	103.09	**27.06%**	2036	1099	**-46.02%**
MCP 3	430	12	112.863	145.494	**28.91%**	2378	1164	**-51.05%**
MCP 4	430	12	118.124	151.534	**28.28%**	2533	1333	**-47.37%**
MCP 5	430	12	148.037	193.85	**30.95%**	2699	1345	**-50.17%**
MCP 6	430	12	126.91	164.312	**29.47%**	2093	1013	**-51.60%**
MCP 7	430	12	119.644	155.157	**29.68%**	2654	1454	**-45.21%**
MCP 8	430	12	116.866	152.167	**30.21%**	2246	1083	**-51.78%**
MCP 9	430	12	123.945	160.06	**29.14%**	2516	1032	**-58.98%**
MCP 10	430	12	137.655	182.831	**32.82%**	2982	1567	**-47.45%**

IV. CONCLUSION

From the results, we can conclude that with vacuum degassing we can increase the MCP resistance by 30%, and also decrease the gain by 50%. The main reason for this can be found in the fact that Pb atoms are distributed homogeneously and after high-temperature vacuum baking it changes. The size of the Pb atoms increases which leads to a decrease in emission layer efficiency of MCP, thus it increases the bulk resistance and decreases the electron gain of MCP. [6.7]

In this way, we can improve channel purity, reduce gas content, stabilize the performance of MCP, and prolong the operating life of the image intensifier tube.

ACKNOWLEDGMENT

We are grateful to Photon Optronics and Sova HD corporations that have created conditions for performing experiments and measuring characteristics of the microchannel plate.

REFERENCES

[1] G.W. Fraseer, J.E. Pearson, J.E. Lees, "Advances in microchannel plate detectors*", Proc. SPIE 982*, pp. 98-107, 1988.

[2] J. L. Wiza, "MICROCHANNEL PLATE DETECTORS" *Nuc. Instrum. Methods*, vol. 162, pp. 587-601, 1979.

[3] D.Borissova, *Night Vision Devices- Modeling and Optimal Design*, Sofia, Bulgaria: Prof. Marin Drinov Publishing House of Bulgarian Academy of Sciences, 2005

[4] "MCP Assembly", Hamamatsu. (n.d.). Retrieved from: https://www.hamamatsu.com/resources/pdf/etd/MCP_TMCP0002E.pdf

[5] A.M. Then, C.G. Pantano, "Formation and behavior of surface layers on electron emission glasses", Journal of Non-Crystalline Solids, vol. 120, no. 1-3, pp. 178-187, Apr. 1990.

[6] Lianxin Zhang, Yiyu Wang, "Electrical performance for MCP after baking, Journal of Changchun Institute of optics Proc. of SPIE, vol. 6621, 3, pp. 44-48,1985.

[7] Jiang, Delong, and Li, Ye and Wu, Kui and Wang, Guozheng and Fu, Shencheng and Wong, Yuki and Duanmu, Qingduo and Tian, Jingquan, "Influence of high-temperature vacuum backing on the performance of Microchannel Plates with an ion barrier film", *Proceedings of SPIE - The International Society for Optical Engineering*, vol. 6621, 2008.

Different Ways to Charging Supercapacitor in WSN Using Solar Cells

Milan Stojanović, *Student Member, IEEE,* Jana Vračar, *Student Member, IEEE,* Ljubomir Vračar

***Abstract*—The supercapacitors are widely used as a primary or secondary energy source in WSN. In this paper, different ways to charge the supercapacitor using solar cells are presented. The charging time for different connection of solar cells at different levels of light intensity is shown. Also, the advantages and disadvantages of using voltage booster are discussed and explained with appropriate results.**

***Index Terms*—Supercapacitor, Solar cell, Charging time, WSN, Voltage booster.**

I. Introduction

Wireless Sensor Network (WSN) is one of the most popular technologies today. This network is composed of nodes, and every node has one or more sensors, a microcontroller, and a radio module for communication with the base station. Powering of the WSN nodes is the main problem in all application because the nodes are usually located in some places where is difficult to carry out their maintenance.

The period during which the WSN node can work completely autonomous (without intervention) represents a lifetime of the WSN node. The initial solution for the power supply of WSN nodes was a battery. It is a good solution from the aspect of energy density and self-discharge current. However, batteries have a finite lifecycle (number of charge and discharge) and therefore their frequent replacement is necessary, and it is a significant limitation for their using in these power supply units. But batteries are necessary in applications that include hundreds of WSN nodes and high rates because of high energy consumption.

If the WSN node is powered by a battery, then its lifetime is determined by the capacity of the battery and energy consumption. Obviously, the lifetime of the WSN node can be extended in two ways, increasing the capacity of the battery or reducing the energy consumption of active elements. The first option can be achieved by energy harvester and the supercapacitor.

II. Increasing Capacity of Storage Unit in WSN

The supercapacitors have been used to increase the power capabilities in WSN nodes. They also have a significant role in other electronics areas even more in commercial products and devices. In some application, which consumes low energy, the battery can be removed and the supercapacitor can be used as the primary energy storage element. The second option is using hybrid systems, storage energy units that have both the battery and the supercapacitor [1]. The supercapacitors are a good solution for storing energy in energy harvesting wireless sensor network nodes (EH-WSNs).

In paper [2] is described power supply unit with the supercapacitor used in combination with a renewable energy source. The paper [3] shows a node with a power supply based on solar cell and the supercapacitor. The estimated lifetime without maintenance, how it is presented in this paper, is 20 years. The other improvements are MPPT (Maximum Power Point Tracking) and PFM (Pulse Frequency Modulation).

The most significant drawback of the supercapacitor is leakage current and self-discharging process described in [4] and [5]. A part of the supercapacitor energy is dissipated on a series resistance which is present because of imperfections in its structure [6]. Also, a power management circuit is needed to provide a balance between harvested and consumed energy over a long period [7]. If the harvested energy is greater than the consumed energy, the power management circuit will charge the supercapacitor. Energy will be used from the supercapacitor if harvested energy is not sufficient.

III. Experimental Setup

The idea of this research is a comparison of different ways to charge the supercapacitor with a solar cell at different levels of light intensity.

The main goal is finding the most effective solution to charge the supercapacitor (470 mF) up to 3.3 V with the different configurations of solar cells whereby all configurations produce the same output power. This voltage level is chosen because this is a working voltage for the numerous microcontrollers, sensors, and radio modules in WSN nodes.

The structure of the supercapacitor implicates that it can not be said with certainty at this moment if the supercapacitor fully charged. Because of that, the time where voltage of the supercapacitor comes up to 3.3 V (charging time) is measured instead of fully charging time.

Two identical solar cells, IXYS 17-04x3 (Fig. 1), were used. The basic parameters of these cells are open circuit voltage, V_{OC}=1.89 V, and short circuit current, I_{SC}=42 mA. It should be noted that these values were obtained with measurements at standard test conditions environment

Milan Stojanović is with Department of Microelectronics, University of Niš, Faculty of Electronic Engineering, Aleksandra Medvedeva 14, 18000 Niš, Serbia, e-mail: milan.stojanovic@elfak.ni.ac.rs

Jana Vračar is with Department of Microelectronics, University of Niš, Faculty of Electronic Engineering, Aleksandra Medvedeva 14, 18000 Niš, Serbia, e-mail: milan.stojanovic@elfak.ni.ac.rs

Ljubomir Vračar is with Department of Microelectronics, University of Niš, Faculty of Electronic Engineering, Aleksandra Medvedeva 14, 18000 Niš, Serbia, e-mail: ljubomir.vracar@elfak.ni.ac.rs

(1000 W/m^2), and their values will be significantly different in real conditions.

Fig. 1. Solar cell IXYS 17-04x3.

These solar cells are part of the IXOLARTM SolarBITs high efficiency solar cells made from monocrystal silicon. Its efficiency is about 17%, and they can work in low light conditions, so they are suitable for WSN nodes and portable instrumentations. The main advantage of used solar cells is small size and they can be easily accommodated in many designs.

In the first configuration, shown in Fig. 2, two solar cells are connected in series, so the output voltage is 3.5 V – 3.6 V in the light range of interest. In this configuration, the supercapacitor can be charging directly from solar cells, without any additional circuits. Between solar cells and the supercapacitor Schottky diode is needed to prevent discharging in the inverse direction in low light conditions. The Zener diode should be placed in parallel with the supercapacitor because the output voltage of solar cells can rise above the critical level in high light conditions.

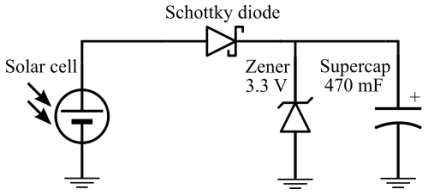

Fig. 2. Electric circuit for charging the supercapacitor with two solar cells connected in series.

The second configuration is a parallel connection of solar cells. In this configuration solar cells produce higher current, so the charging time of the supercapacitor should be shorter than in series configuration. But, in this case, the output voltage of solar cells is not sufficient (1.8 V) for charging the supercapacitor, so the voltage booster (booster) must be inserted in the circuit (Fig. 3). The booster can produce higher voltage on his output than the input voltage is. This concept is very widely used in many applications with multiple energy harvester sources [8].

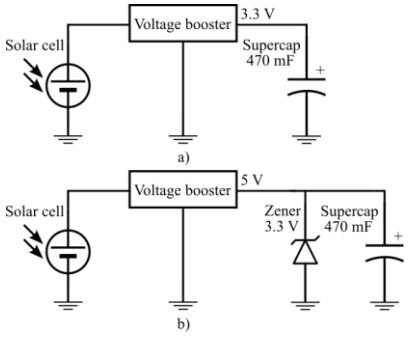

Fig. 3. Electric circuit for charging the supercapacitor with two solar cells connected in parallel. a) The output voltage of the booster at 3.3 V; b) The output voltage of the booster at 5 V.

In case a) the output voltage of the booster is 3.3 V and the supercapacitor is connected directly to this voltage without any additional component. The Zener diode is not necessary because the output voltage of the booster is regulated and independent from changes in input voltage.

The second way is charging the supercapacitor with a voltage that is higher than it is needed. In this case it is 5 V, like it is shown on b) part of Fig. 3. The Zener diode is necessary here.

The idea is to determine whether the charging time of the supercapacitor decrease when the output voltage of the booster rises.

One more way is a series connection of cells and charging the supercapacitor with the booster. In this case, the booster is not needed but, like in the former case, the idea is to measure charging time at a higher voltage with the same configuration.

In this research was used high-efficiency, fixed frequency, DC-DC voltage booster MCP1640 [9]. It can be used for power supply with batteries and energy harvester sources. The output voltage range is from 2 V to 5.5 V and the input voltage range is 0.35 V < V_{OUT} < 5.5 V, with the start-up voltage of 0.65 V. This circuit can automatically switch over between PWM and PFM mode to maximize efficiency. The output voltage can be easily adjusted by selecting just two resistor values (R_1 and R_2). R_1 is a resistor connected between FB pin and ground pin and R_2 is the resistor connected between FB pin and OUT pin. The output voltage can be expressed by equation 1:

$$V_{OUT} = V_{FB} (1 + R_1/R_2), \quad (1)$$

where V_{FB} is a fixed voltage reference of 1.21 V.

More practical way for setting the output voltage, shown in Fig. 4, can be realized using a potentiometer instead of resistors R_1 and R_2.

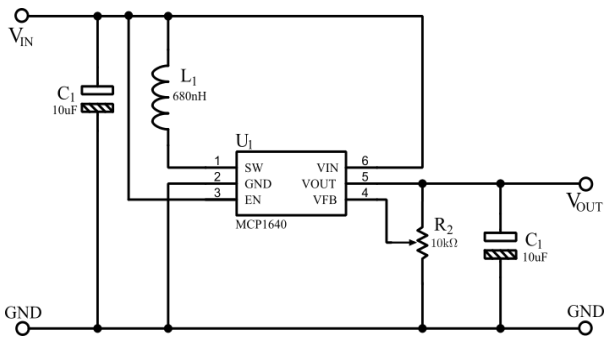

Fig. 4. Simplified electronic circuit with voltage booster MCP1640.

IV. Results

The most simplified way to charge the supercapacitor, of all presented, by using solar cells is one in Fig. 2. The charging curves of the supercapacitor based on this configuration are shown in Fig. 5.

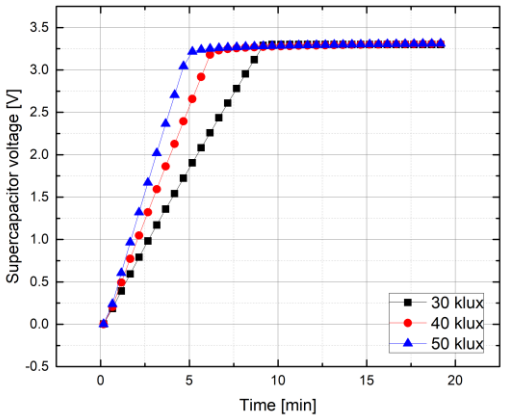

Fig. 5. Charging time of the supercapacitor in case of a series connection of solar cells. These results are obtained using the circuit shown in Fig. 2.

It needs several minutes for charging the supercapacitor up to 3.3 V and the charging curves have different slope at different levels of light intensity. The curve has a higher slope at a higher level of light intensity and it confirms theoretical claims. The reason for that is the fact that solar cells produce more output power at a higher level of light intensity. In other words, if the level of light intensity rises then charging time decreases.

The charging time of the supercapacitor is longer when the solar cells are connected in parallel although they produce higher current in that case. The curves in Fig. 6 confirm that.

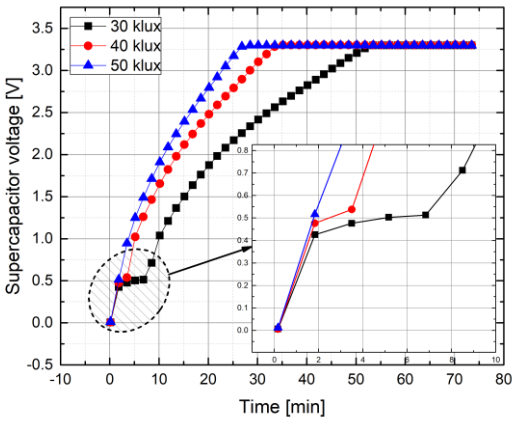

Fig. 6. Charging time of the supercapacitor in case of a parallel connection of solar cells with MCP1640 booster. The output voltage of the booster is 3.3 V. These results are obtained using the circuit shown in Fig. 3. a).

The booster used in this case helps to get sufficient voltage level to charging the supercapacitor (input voltage is 1.8 V), and without it, the charging process will not be possible. However, the voltage booster consumes energy and can not deliver all of the energy produced by solar cells to the supercapacitor. It is a reason because the charging time is much longer in this case than in the case without the booster.

The moment when the booster becomes active is shown on the circled and enlarged part of Fig. 6. Like can be seen, it is needed some time for the booster to accumulate enough energy for generating a certain voltage level on its output. This time is longer at a lower level of light intensity because of lower input energy. In Fig. 7 is shown voltage level (PFM form) on the SW pin of the booster when the circuit is in the active state. In this case, the input voltage is boosted and passed to the output pin.

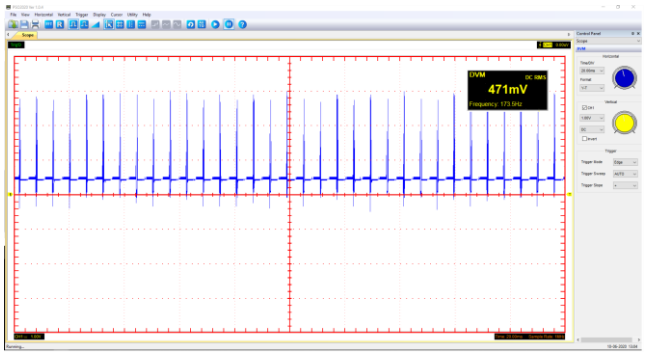

Fig. 7. The voltage on the SW pin while the MCP1640 booster is in the active state.

Like already said, the second way to charge the supercapacitor with the booster is to set the output voltage of the booster to a higher level than it is necessary. With a higher output voltage of the booster (potential difference between the booster and the supercapacitor), it can be expected that the charging time of the supercapacitor will be shorter. However, this claim is valid only if the intensity of the current is still constant. It can not be achieved with the booster and the curves in Fig. 8 confirm that.

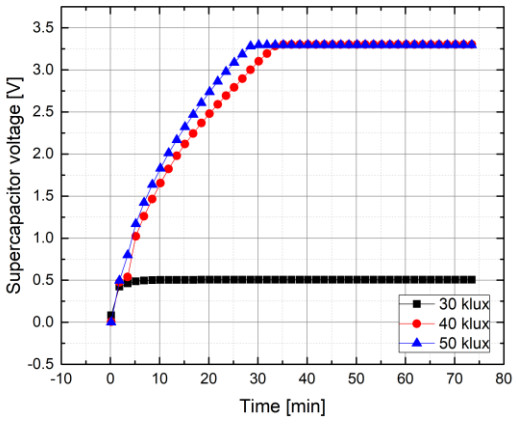

Fig. 8. Charging time of the supercapacitor in case of a parallel connection of the solar cells with MCP1640 booster. The output voltage of the booster is 5 V. These results are obtained using the circuit shown in Fig. 3. b).

The charging time at 40 klux and 50 klux is several minutes longer than in the case when the output voltage of the booster is 3.3 V. Actually, this can be explained as a consequence of the law of conservation of energy. If the input power is constant then the output power will be constant also. The consequence of that is smaller output current with increasing the output voltage and because the output current is smaller, the more time is needed to charge the supercapacitor.

The additional problem in this case is occurred at a low level of light intensity conditions because of the low current that solar cells produce. A low current means low input power and the booster can not be activated (Fig. 9). The unregulated frequency of the PFM signal on the SW pin and amplitude of this signal indicates a deficiency of the energy

to produce a high output voltage. Thus, the output current is the same as input and is not sufficient for charging the supercapacitor, and it will be charged only up to 0.5 V, approximately.

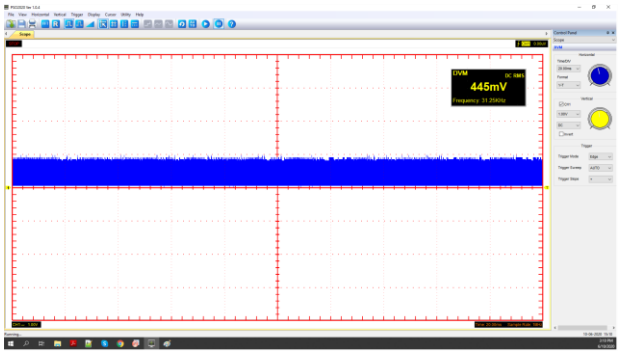

Fig. 9. The voltage on the SW pin while the MCP1640 booster is in the inactive state. Time base and the voltage per division are equal as on Fig 7.

Fig. 10 and Fig. 11 show the summarized comparisons of the charging time of the supercapacitor for different circuit configurations at two different levels of light intensity.

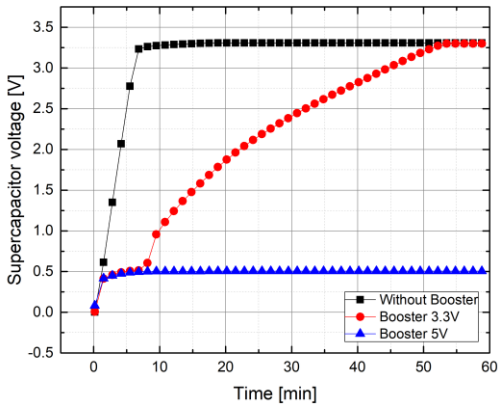

Fig. 10. Comparison of charging time of the supercapacitor for different circuit configurations at 30 klux.

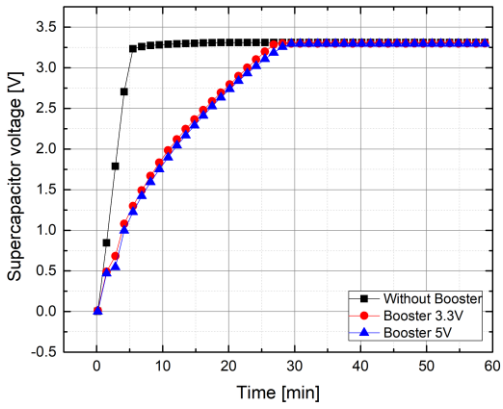

Fig. 11. Comparison of charging time of the supercapacitor for different circuit configurations at 50 klux.

V. Conclusion

Based on the obtained and presented results it can be resumed that the best solution for charging the supercapacitor using solar cells is the circuit without the booster. That is because there is not an additional waste of energy on the booster circuit and almost all produced energy goes to the supercapacitor.

On the other hand, when the combination of solar cells has a smaller output voltage then it is necessary, the booster is a good solution.

One should keep in mind that the booster consumes some part of produced energy so the charging time of the supercapacitor will be longer. Also, a certain amount of energy and time is needed to activate the booster. It extends the charging time of the supercapacitor and it can be a problem at a lower level of light intensity. If the output voltage of the booster rises, the output current will decrease and the charging time will be longer, so the output voltage of the booster should not be higher than it is needed when a source is a solar cell or some other energy harvester with dependent output current.

Acknowledgment

This work has been supported by the Ministry of Education, Science and Technological Development of the Republic of Serbia, under Grant TR32026.

References

[1] M. T. Penella-López, M. Gasulla-Forner, “Powering Autonomous Sensors”, Springer Dordrecht Heidelberg London New York, 2011.

[2] P. Ševčík, O. Kovář, “Power unit based on supercapacitors and solar cell module”, 1st International Virtual Scientific Conference, June, 10. - 14. 2013.

[3] F. Simjee and P. H. Chou, "Everlast: Long-life, Supercapacitor-operated Wireless Sensor Node," ISLPED'06 Proceedings of the 2006 International Symposium on Low Power Electronics and Design, Tegernsee, pp. 197-202, 2006.

[4] R. de Fazio, D. Cafagna, G. Marcuccio, P. Visconti, "Limitations and Characterization of Energy Storage Devices for Harvesting Applications." Energies 13, no. 4: 783, MDPI, 2020.

[5] A. S. Weddell, G. V. Merrett, T. J. Kazmierski and B. M. Al-Hashimi, "Accurate Supercapacitor Modeling for Energy Harvesting Wireless Sensor Nodes," in IEEE Transactions on Circuits and Systems II: Express Briefs, vol. 58, no. 12, pp. 911-915, Dec. 2011.

[6] T.Nhan Le, “Global power management system for self-powered autonomous wireless sensor node”, Ph.D. dissertation, Traitement du Signal et Télécommunications, Université Rennes, Rennes, France, 2014.

[7] T. N. Le, A Pegatoquet, B. Olivier, O. Sentieys, “Multi-Source Power Manager for Super-Capacitor based Energy Harvesting Wireless Sensor Networks”, Proceedings of the 1st International Workshop on Energy Neutral Sensing Systems, 2013.

[8] C. Shi, B. Miller, K. Mayaram, and T. Fiez, A Multiple-Input Boost Converter for Low-Power Energy Harvesting, IEEE Transactions on Circuits and Systems—II: Express Briefs, Vol. 58, No. 12, December 2011.

[9] “MCP1640/B/C/D, 0.65V Start-Up Synchronous Boost Regulator with True Output Disconnect or Input/Output Bypass Option”, Microchip Technology Inc., 2010

Modelovanje promena napona praga p-kanalnih VDMOS tranzistora snage tokom NBT naprezanja

Nikola Mitrović, *Student Member, IEEE*, Danijel Danković, *Member, IEEE*, Zoran Prijić, *Member, IEEE*, Ninoslav Stojadinović, *IEEE, Life Fellow*

***Apstrakt*—U ovom radu prikazana je analiza eksperimentalnih rezultata nestabilnosti napona praga p-kanalnih VDMOS tranzistora snage IRF9520 podvrgnutih temperaturnom naprezanju sa negativnom polarizacijom gejta, dok je glavni deo istraživanja modelovanje promene napona praga prema dobijenim eksperimentalnim rezultatima. Osmišljeno je i prikazano elementarno kolo za modelovanje i statičkog i impulsnog naprezanja tranzistora, kao i proračun vrednosti ključnih elemenata kola. Na kraju je data uporedna analiza eksperimentalnih i modelovanih rezultata.**

***Ključne reči*—VDMOS transistor snage; NBTI; napon praga; modelovanje;**

I. Uvod

Nestabilnosti usled naponsko temperaturnih naprezanja sa negativnom polarizacijom gejta (skr. NBTI, od eng. Negative Bias Temperature Instability) MOS tranzistora postaju jedna od sve važnijih tema prilikom proučavanja pouzdanosti komponenata. Ova nestabilnost se manifestuje kroz pomeranje vrednosti napona praga usled NBT naprezanja, i samim tim direktno utiče na period pouzdanog rada komponenata. NBTI efekti se javljaju pri naprezanju p-kanalnih MOS tranzistora negativnim naponima na gejtu, kojima odgovaraju polja u oksidu gejta od 2-6 MV/cm, na povišenim temperaturama, u opsegu 100-250˚C [1-3].

Mikroskopski mehanizmi NBTI još uvek nisu u potpunosti objašnjeni. Ipak, poznato je da se NBTI efekti ispoljavaju kroz smanjenje transkonduktanse komponenata (g_m), smanjenje apsolutne struje drejna (I_{Dsat}) i promenu napona praga (ΔV_T) [2]. Sa stanovišta praktične primene najinteresantnije su promenama napona praga pri impulsnom NBT naprezanju, pa je ovo istraživanje i od najvećeg interesa. Pogotovo je bitan za procene perioda pouzdanog rada komponenata, jer su NBTI efekti označeni kao kritični ograničavajući faktori koju utiču na period pouzdanog rada [1-5].

U prethodnim godinama izvršena su brojna istraživanja kako bi se proučili suštinski mehanizmi NBTI efekata na MOS tranzistore, kako bi se razvile nove merne metode za merenje ovih efekata i kako bi se razložile pojedinačne komponente degradacije [4-6]. Pokazano je da NBTI model koji oponaša degradaciju usled statičkog naprezanja može da napravi pogrešnu procenu pouzdanosti u odnosu na stvarnu degradaciju usled impuslnog naprezanja, koja je zastupljenija u praktičnoj primeni. Modelovanje degradacije usled impulsnog naprezanja i dalje ostaje izazovan zadatak, jer NBTI efekti zavise kako od napona i temperature tako i od učestanosti i od faktora ispune impulsnog napona koji vrši naprezanje [7-11].

U ovom radu analizirani su efekti kod p-kanalnih VDMOS (od izraza: Vertical Double Diffused Metal Oxide Semiconductor) tranzistora snage [12] IRF9520 [13] koji su podvrgnuti NBT naprezanju. Takođe, kako bi se predvideo period pouzdanog korišćenja komponenata, izvršeno je i modelovanje napona praga na osnovu raspoloživih eksperimentalnih podataka dobijenih tokom NBT naprezanja [14-17].

Naša ranija istraživanja bavila su se efektima NBTI kod p-kanalnih VDMOS tranzistora snage. Ovaj tip tranzistora je izuzetno pogodna komponenta za primene u prekidačkim izvorima napajanja, zbog svojih superiornih prekidačkih karakteristika [10], pa je iz tih razloga i značajno modelovanje promena napona praga pri impulsnom naprezanju.

II. Eksperiment i analiza rezultata

Sa ciljem dobijanja adekvatnih rezultata za modelovanje ΔV_T, izvršeni su eksperimenti nad različitim grupama tranzistora koji su podvrgnuti NBT naprezanju pri tipičnim uslovima (-45 V, 175˚C). Naprezanja su vršena jednosmernim i impulsnim naponima na gejtu sa različitim faktorima ispune. U ovom radu, akcenat je na statičkom naprezanju, kao i impulsnom naprezanju, gde je faktor ispune impulsnog napona 50%, odnosno gde je vreme trajanja visokog i niskog naponskog nivoa jednako [7-9, 18].

Kao uzorci u eksperimentu korišćeni su komercijalni p-kanalni VDMOS tranzistori snage IRF9520, koji su realizovani u standardnoj poli-Si gejt tehnologiji, sa heksagonalnom ćelijskom strukturom (1650 ćelilja) i oksidom

Nikola Mitrović – Univerzitet u Nišu, Elektronski fakultet, Aleksandra Medvedeva 14, 18000 Niš, Srbija (e-mail: nikola.i.mitrovic@elfak.ni.ac.rs).

Danijel Danković – Univerzitet u Nišu, Elektronski fakultet, Aleksandra Medvedeva 14, 18000 Niš, Srbija (e-mail: danijel.dankovic@elfak.ni.ac.rs).

Zoran Prijić – Univerzitet u Nišu, Elektronski fakultet, Aleksandra Medvedeva 14, 18000 Niš, Srbija (e-mail: zoran.prijic@elfak.ni.ac.rs).

Ninoslav Stojadinović – Univerzitet u Nišu, Elektronski fakultet, Aleksandra Medvedeva 14, 18000 Niš; Srpska akademija nauka i umetnosti (SANU) – Ogranak u Nišu, Univerzitetski trg 2, 18000 Niš, Srbija (e-mail: ninoslav.stojadinovic@elfak.ni.ac.rs).

gejta nominalne debljine 100 nm. Maksimalna struja drejna ovih tranzistora je 6.8 A, a vrednost napona praga izmerena pre naprezanja bila je V_{TO}=-3.6 V. Komponente su montirane u plastična kućišta TO-220 [13].

Jedna grupa ispitivanih uzoraka naprezana je kontinualnim negativnim naponima na gejtu od -45 V (pri čemu su sors i drejn bili uzemljeni) na temperaturi od 175˚C u ukupnom trajanju od 12 sati. Druga grupa uzoraka podvrgnuta je impulsnim naponsko temperaturnim naprezanjima frekvencije 10 kHz (periode 100 μs) i faktora ispune 50%, sa identičnim vrednostima napona, temperature i vremena NBT naprezanja kao i kod prve grupe uzoraka. Eksperimentalni rezultati prikazani su na slici 1.

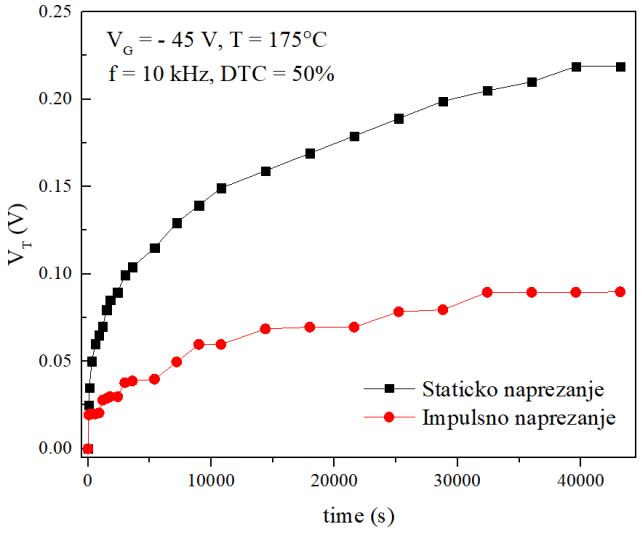

Sl. 1. Eksperimentalni rezultati za ΔV_T dobijeni tokom statičkog i impulsnog NBT naprezanja p-kanalnih VDMOS tranzistora IRF9520.

U gotovo svim dosadašnjim istraživanjima NBTI efekata kod p-kanalnih MOS tranzistora proizvedenih u različitim tehnologijama, nezavisno od toga da li se radi o statičkom ili o impulsnom naprezanju, dobijena je promena napona praga po zakonu t^n, gde je n < 1 [1-3,18-20]. Takođe, dobijeni rezultati ukazuju na to da je ΔV_T znatno izraženije kod statičkog nego kod impulsnog naprezanja, kao i pri višim naponima i/ili temperaturama [9, 11, 18, 20].

Prilikom impulsnog naprezanja, grafički ilustrovano na slici 2, tokom visokog naponskog nivoa (označeno kao ON vreme), efekat naprezanja isti je kao i prilikom statičkog naprezanja. Sa druge strane, tokom niskog naponskog nivoa (OFF vreme), dolazi do delimičnog oporavka degradacije napona praga nastale usled naprezanja. Zbog toga, promenu napona praga po impulsu moguće je podeliti na dve komponente, reverzibilnu i ireverzibilnu [10]. Reverzibilna je označena sa ΔV_{TR}, i predstavlja deo koji se, nakon prestanka delovanja visokog naponskog nivoa napona na gejtu, oporavi, dok ireverzibilna komponenta, označena sa ΔV_{TIR}, predstavlja deo degradacije koji se ne oporavi.

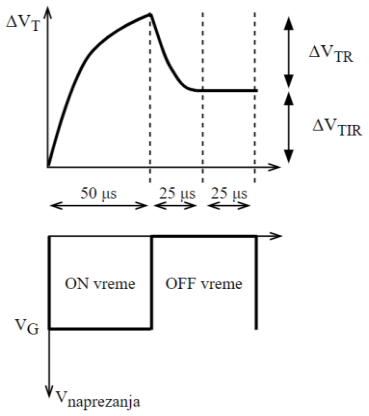

Sl. 2. Grafička ilustracija promene napona praga pod uticajem jednog impulsa pri impulsnom NBT naprezanju.

Prethodni rezultati naših istraživanja istakli su postojanje karakteristične vremenske konstante (25 μs) koja je povezana sa oporavkom napona praga pri degradaciji impulsnim naprezanjem [7-10, 18, 22]. Pokazano je da je prilikom impulsnog naprezanja, tokom trajanja niskog naponskog nivoa impulsnog napona za naprezanje (a nakon prestanka delovanja visokog nivoa), vreme od 25 μs dovoljno da se odstrani najveći deo reverzibilne komponente.

III. Modelovanje ΔV_T

Bilo je više pokušaja modelovanja ΔV_T [14-17, 23, 24] tokom NBT naprezanja. Sa ciljem unapređenja na polju modelovanja, u ovom radu predloženo je elementarno kolo za modelovanje. Kolo je inicijalno osmišljeno za statičko naprezanje, a onda je u električnom smislu prošireno za impulsno naprezanje.

Kako se napon praga menja po stepenom zakonu (t^n), a koji se za male intervale vremena poklapa sa eksponencijalnim zakonom, kolo za modelovanje sastoji se iz kondenzatora C koji se puni preko otpornika R, kao što je ilustrovano na slici 3 (otpornik R_C i kondenzator C_1). Ovde je iskorišćena osobina kondenzatora da se, tokom punjenja, napon na njemu povećava eksponencijalno. Promena napona na kondenzatoru odgovara promeni ΔV_T, i računa se kao:

$$V_C = V_S \left(1 - e^{-\frac{t}{R_C C}}\right) \qquad (1)$$

Gde je V_C trenutna vrednost napona, V_S napon koji V_C dostiže u beskonačnosti. Računanjem vrednosti kapacitivnosti kondenzatora i otpornosti otpornika, dolazi se do vrednosti koje modeluju ΔV_T prilikom statičkog naprezanja. Kako postoji jedna jednačina, a dve nepoznate, potrebno je izabrati jednu promenljivu, kako bi se izračunala druga. Ovakav tip pretpostavke neophodan je prilikom modelovanja, a vrednost se obično bira na osnovu iskustva.

Međutim, kako su ove komponente zastupljene u primenama gde do izražaja dolaze njihove prekidačke osobine, efekti impulsnog naprezanja VDMOS tranzistora su

od znatno većeg interesa u odnosu na efekte statičkog naprezanja [10]. Zbog toga je akcenat na modelovanju NBTI usled impulsnog naprezanja.

Kod impulsnog naprezanja, rastući deo krive mikrosignala (prikazanog na slici 4), nastao za vreme trajanja visokog naponskog nivoa impulsnog napona (ON vreme) za naprezanje predstavljen je kao punjenje kondenzatora C_1 preko otpornika R_C (odgovara prvoj polovini periode). Drugi deo krive istog mikrosignala (OFF vreme) podeljen je na dva dela, na opadajući deo i konstantni deo. Opadajući deo predstavljen je kao pražnjenje kondenzatora C_1 preko otpornika R_D, dok je za vreme konstantnog dela potrebno zaustaviti pražnjenje. Kako eksperimentalni rezultati ukazuju na to da je nakon prestanka delovanja visokog naponskog nivoa, vreme od 25 μs dovoljno da se oporavi najveći deo reverzibilne komponente, pražnjenje kondenzatora C_1 treba omogućiti samo tokom trajanja navedene vremenske konstante.

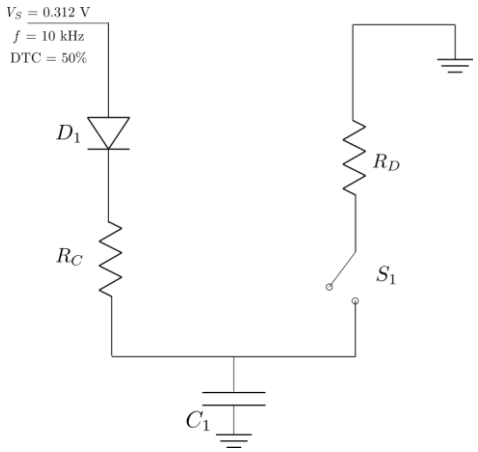

Sl. 3. Električno kolo za modelovanje ΔV_T pri impulsnom NBT naprezanju. Napon V_s određen je korišćenjem modela rastegnute eksponencijalne funkcije kao što je demonstrirano u [17].

Impulsni napon se prosleđuje kondenzatoru C_1 preko otpornika R_C i idealne diode D_1, tako da se kondenzator puni. Sa druge strane, kondenzator se prazni preko otpornika R_D. Dioda D_1 obezbeđuje da se kondenzator prazni samo preko otpornika R_D, a ne i preko otpornika R_C, odnosno, ima isključivo usmeračku ulogu. Vrlo bitan deo kola je naponski kontrolisan prekidač, S_1, koji je povezan u grani kola za pražnjenje. Kako je cilj modela omogućiti pražnjenje samo tokom 25 μs, prekidač treba kontrolisati signalom koji je sinhronizovan sa impulsnim signalom za naprezanje, tako da omogući pražnjenje kondenzatora u prvih 25 μs nakon prestanka trajanja visokog naponskog nivoa signala za impulsno naprezanje. Ovaj proces selektivnog otvaranja prekidača treba ponoviti prilikom svake periode impulsnog naprezanja. Na ovaj način, cilj je da napon na kondenzatoru V_C odgovara vrednosti ΔV_T koje je rezultat impulsnog NBT naprezanja. Slična električna kola za modelovanje određenih promena napona već su prikazana u [14-17, 23, 25], odakle je i potekla osnovna ideja. Međutim, osnovna modifikacija je uvođenje kontrolisanog prekidača S_1, a sve zbog specifične vremenske konstante od 25 μs koja je uočena kod VDMOS tranzistora snage [16, 17].

Kako bi se omogućilo poklapanje modelovanih i eksperimentalnih rezultata, potrebno je izračunati odgovarajuće vrednosti kapacitivnosti i otpornosti. Prilikom računanja ovih vrednosti, treba obratiti pažnju na evoluciju mikrosignala. Eksponencijalna priroda t^n se, između ostalog, ogleda u tome što je, prilikom impulsnog naprezanja, priraštaj ΔV_T po impulsu najveći na početku, a onda vremenom, priraštaj po impulsu opada [18-20].

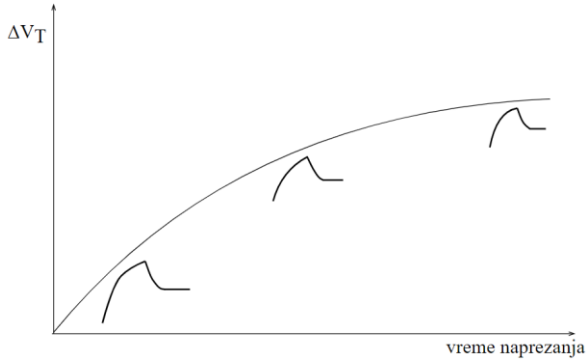

Sl. 4. Grafička ilustracija promene priraštaja ΔV_T po vremenu pri impulsnom NBT naprezanju.

Za modelovanje impulsnog naprezanja, proračunom bi trebalo doći do tri vrednosti, R_C, R_D i C_1. Takođe, proračun treba da isprati promenu priraštaja ΔV_T po impulsu, odnosno da na početku ΔV_T bude najveće, a onda sve manje i manje.

Za t = 12 sati impulsnog naprezanja, ΔV_T se promeni od 0 V do 0.0895 V. Kako je učestanost impulsnog napona za naprezanje 10 kHz, za vreme t, na gejt VDMOS tranzistora dođe $4.32 \cdot 10^9$ impulsa. Odatle, srednja vrednost priraštaja ΔV_T po impulsu je $2.07 \cdot 10^{-10}$ V. Ova srednja vrednost priraštaja dostiže se u nekom trenutku razvoja degradacije napona praga. Za računanje položaja tačke u kojoj razvoj dostiže srednju vrednost iskorišćena je Lagranžova teorema [26]. Tačka u kojoj razvoj dostiže ovu vrednost je tačka u kojoj je tangenta paralelna pravoj koju formiraju početna i krajnja tačka razvoja ΔV_T, kao što je ilustrovano na slici 5.

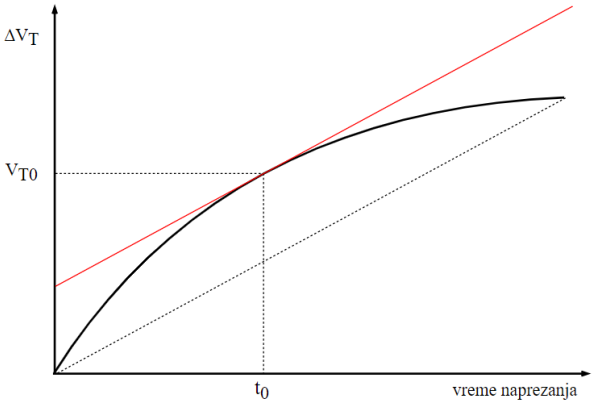

Sl. 5. Grafička ilustracija određivanja tačke u kojoj priraštaj ΔV_T po impulsu ima srednju vrednost za ceo interval (V_{T0}).

Grafičkom analizom utvrđeno je da se srednja vrednost priraštaja dostiže nakon 14430 s i da promena napona praga u tom trenutku iznosi 0.069 V. Do tada, naprezanjem je isporučeno $1.443 \cdot 10^8$ impulsa. Ukoliko se pretpostavi da ΔV_T dostiže vrednost V_{T0} nakon n impulsa, nakon $n+1$ impulsa, dostići će vrednost približno $V_{T0} + \Delta V_{Tsred}$. Ovo su dve tačke na osnovu kojih je moguće izračunati R_C i R_D. Ilustracija srednjeg impulsa prikazana je na slici 6.

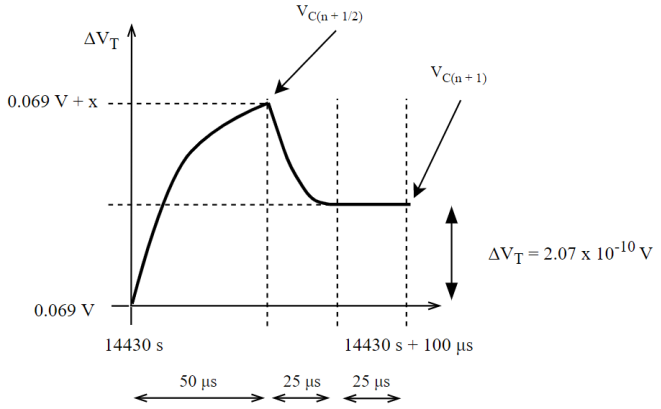

Sl. 6. Analiza odmerka promene ΔV_T pri impulsu koji ima srednju vrednost za ceo razvoj promene napona praga.

Kako odziv kondenzatora nije isti kada je kondenzator prazan i kada na njemu već postoji neki napon, navedeni interval opisan jednačinama je:

$$V_{C(n+\frac{1}{2})} = V_{C(n)} + \left(V_{S_{50\%}} - V_{C(n)}\right)\left(1 - e^{-\frac{t_C}{R_C C}}\right) \quad (2)$$

$$V_{C(n+1)} = V_{C(n+\frac{1}{2})}\, e^{-\frac{t_D}{R_D C}} \quad (3)$$

Rešavanjem sistema jednačina, dolazi se do nepoznatih vrednosti otpornosti R_C i R_D. Ove vrednosti date su u tabeli I.

TABELA I
VREDNOSTI KARAKTERISTIČNIH ELEMENATA KOLA ZA MODELOVANJE

Statičko naprezanje	Impulsno naprezanje	
$R_C = 3.6 \cdot 10^7\ \Omega$	$R_C = 3.6 \cdot 10^5\ \Omega$	$R_D = 2.43 \cdot 10^5\ \Omega$
$C_1 = 1$ mF		

Na osnovu izračunatih vrednosti otpornosti i jednačina (2) i (3), moguće je izračunati priraštaj degradacije napona praga pri svakom impulsu. U tabeli II su date vrednosti priraštaja ΔV_T po određenim karakterističim impulsima. Na slici 7 su prikazani uporedno izmereni i modelovani rezultati.

TABELA II
VREDNOSTI PRIRAŠTAJA PROMENA NAPONA PRAGA PO KARAKTERISTIČNIM IMPULSIMA

Redni broj impulsa	Priraštaj po impulsu [V]	Ukupna promena [V]
1	$16.82 \cdot 10^{-9}$	$16.82 \cdot 10^{-9}$
2	$16.81 \cdot 10^{-9}$	$33.63 \cdot 10^{-9}$
3	$16.79 \cdot 10^{-9}$	$50.42 \cdot 10^{-9}$
⋮		
$1.443 \cdot 10^8 - 1$	$2.07 \cdot 10^{-10}$	0.0689999932043591
$1.443 \cdot 10^8$	$2.07 \cdot 10^{-10}$	$6.9 \cdot 10^{-2}$
$1.443 \cdot 10^8 + 1$	$2.06 \cdot 10^{-10}$	0.0690000020671664
⋮		
$4.32 \cdot 10^9 - 2$	$9 \cdot 10^{-14}$	0.08949999999982
$4.32 \cdot 10^9 - 1$	$9 \cdot 10^{-14}$	0.08949999999991
$4.32 \cdot 10^9$	$9 \cdot 10^{-14}$	0.0895

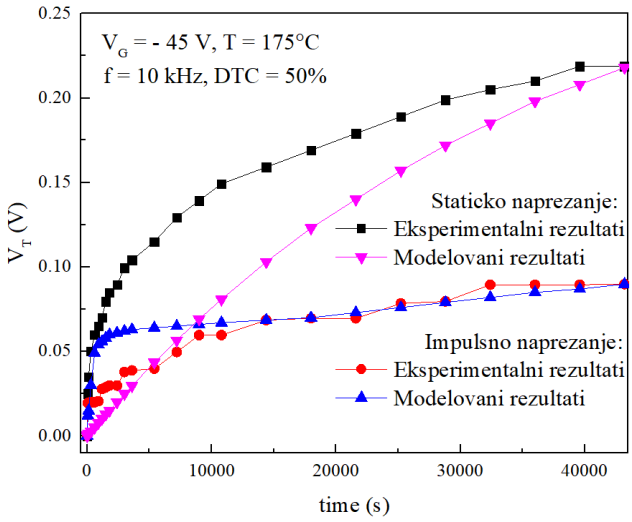

Sl. 7. Poređenje eksperimentalnih i modelovanih rezultata statičkog i impulsnog NBT naprezanja p-kanalnih VDMOS tranzistora IRF9520.

Kriva eksperimentalnih rezultata i kriva modelovanih rezultata prilikom modelovanja statičkog naprezanja, imaju sličan oblik, mada je u srednjim delovima krive primetno veće neslaganje. Sa druge strane, kriva eksperimentalnih i kriva modelovanih rezultata prilikom impulsnog naprezanja takođe pokazuje neslaganje, ali u početnom delu naprezanja i u manjem obliku u odnosnu na statičko naprezanje. U većem delu vremena, eksperimentalna i modelovana kriva impulsnog naprezanja se gotovo poklapaju. Kako je od većeg interesa za predviđanje pouzdanosti bitnije poklapanje modela za veće vremenske intervale prikazan model daje odgovarajuće rezultate. Osim toga, VDMOS tranzistori se uglavnom koriste u impulsnom režimu rada. Zbog toga, poklapanje eksperimentalnih i modelovanih rezultata pri impulsnom naprezanju ima veći značaj. Pogotovo poklapanje za veće vremenske intervale, zbog određivanja perioda pouzdanog rada.

IV. ZAKLJUČAK

U radu je prikazano kolo za modelovanje promena napona praga VDMOS tranzistora pri statičkom i impulsnom naprezanju. Modelovanje je izvršeno na osnovu eksperimentalnih rezultata. Prostor za unapređenja modela se nalazi se u modelovanju promena usled impulsnog naprezanja kada je vreme trajanja niskog naponskog nivoa manje od karakteristične vremenske konstante od 25 μs. Dalje istraživanje će biti usmereno na razvijanje modela koji bi za izabrane vrednosti učestanosti i faktora ispune impulsnog napona za naprezanje mogao da verodostojno prikaže degradaciju napona praga i izvrši projekciju perioda pouzdanog rad.

ZAHVALNICA

Ovaj rad je podržan od strane Ministarstva prosvete, nauke i tehnološkog razvoja Republike Srbije i od strane Srpske akademije nauka i umetnosti - SANU.

LITERATURA

[1] J.H. Stathis, S. Zafar, „The negative bias temperature instability in MOS devices: A Review“, *Microelectron. Reliab.*, 2006, vol. 46, pp. 270-286.

[2] D.K. Schroder and J.A. Babcock, „Negative bias temperature instability: Road to cross in deep submicron silicon semiconductor manufacturing“, *J. Appl. Phys.*, 2003, vol. 94, pp. 1-18.

[3] S. Ogawa, M. Shimaya, and N. Shiono, „Interface-trap generation at ultrathin SiO2 (4-6 nm)-Si interfaces during negative-bias temperature aging“, *J. Appl. Phys.*, 1995, vol. 77, pp. 1137-1148.

[4] S. Mahapatra, N. Goel, S. Desai, S. Gupta, B. Jose, S. Mukhopadhyay, K. Joshi, A. Jain, A. E. Islam, M. A. Alam, „A Comparative Study of Different Physics-Based NBTI Models“, *IEEE Trans. Electron Devices*, vol. 60, no. 3, pp. 901-916, 2013.

[5] T. Grasser, Th. Aichinger, G. Pobegen, H. Reisinger, P.-J. Wagner, J. Franco, M. Nelhiebel, and B. Kaczer, „The ‘permanent’ component of NBTI: Composition and annealing“, in Proc. IEEE Int. Reliab. Phys. Symp. (IRPS2011), Monterey, CA (USA), 2011, 6A.2.1 - 6A.2.9.

[6] D. Danković, I. Manić, S. Djorić-Veljković, V. Davidović, S. Golubović and N. Stojadinović, „NBT stress-induced degradation and lifetime estimation in p-channel power VDMOSFETs“, *Microelectron. Reliab.*, 2006, vol. 46, pp. 1828-1833.

[7] D. Danković, N. Stojadinović, Z. Prijić, I. Manić and A. Prijić, „Recoverable and Permanent Components of V_T Shift in Pulsed NBT Stressed P-Channel Power VDMOSFETs“, in Proc. 29th Int. Conf. on Microelectronics (MIEL 2014), Belgrade (Serbia), May 2014, pp. 297-300.

[8] D. Danković, N. Stojadinović, Z. Prijić, I. Manić, V. Davidović, A. Prijić, S. Djorić-Veljković, S. Golubović, „Analysis of recoverable and permanent components of threshold voltage shift in NBT stressed p-channel power VDMOSFET“, *Chinese Phys. B*, vol. 24, pp. 106601-1, 2015.

[9] D. Danković, I. Manić, A. Prijić, S. Djorić-Veljković, V. Davidović, N. Stojadinović, Z. Prijić and S. Golubović, „Negative bias temperature instability in p-channel power VDMOSFETs: recoverable versus permanent degradation“, *Semicond. Sci. Technol.*, vol. 30, p. 1056009 (9pp), 2015.

[10] D. Danković, I. Manić, V. Davidović, A. Prijić, M. Marjanović, A. Ilić, Z. Prijić and N. Stojadinović, „On the Recoverable and Permanent Components of NBTI in p-Channel Power VDMOSFETs“, *IEEE Trans. Device Mater. Reliab.*, vol. 16, no. 4, pp. 522-531, 2016.

[11] T. Nigam, „Pulse-stress dependence of NBTI degradation and its impact on circuits“, *IEEE Trans. Device Mater. Reliab.*, vol. 8, no. 1, pp. 72 - 78, 2008.

[12] V. Benda, J. Gowar, D. Grant, *Power Semiconductor Devices*, John Wiley & Sons, New York, 1999.

[13] IRF9520N Data sheet, Int. Rectifier 1998, www.irf.com

[14] I. Manić, D. Danković, N. Stojadinović „Threshold voltage shifts modeling during the NBT stressing and annealing in p-channel power VDMOSFETs“, in Proc. 56th ETRAN Conference, Zlatibor, June 11-14, 2012.

[15] D. Danković, I. Manić, N. Stojadinović, Z. Prijić, S. Djorić-Veljković, V. Davidović, A. Prijić, A. Paskaleva, D. Spassov, and S. Golubović, „Modelling of Threshold Voltage Shift in Pulsed NBT Stressed P-Channel Power VDMOSFETs“, in Proc. 30th Int. Conf. on Microelectronics (MIEL 2017), Nis (Serbia), October 2017, pp. 297-300.

[16] N. Mitrović, D. Danković, Z. Prijić, N. Stojadinović, „Modelling of ΔVT in NBT Stressed P-Channel Power VDMOSFETs“, in Proc. 31st Int. Conf. on Microelectronics (MIEL 2019), Nis (Serbia), September 2019, pp. 177-180.

[17] D. Danković, N. Mitrović, Z. Prijić, N. Stojadinović, „Modeling of NBTS Effects in P-Channel Power VDMOSFETs“, *IEEE Trans. Device Mater. Reliab.*, vol. 20, pp. 204-213, 2020.

[18] A. Prijić, D. Danković, Lj. Vračar, I. Manić, Z. Prijić, N. Stojadinović, „A method for negative bias temperature instability (NBTI) measurements on power VDMOS transistors“, *Meas. Sci. Technol.*, vol. 23, pp. 8, 2012.

[19] K. Jeppson and C. Svensson, „Negative bias stress of MOS devices at high electric fields and degradation of MNOS devices“, *J. Appl. Phys.*, vol. 48, pp. 2004–2014, Jun. 1977.

[20] N. Stojadinović, D. Danković, S. Djorić-Veljković, V. Davidović, I. Manić, S. Golubović, „Negative bias temperature instability mechanisms in p-channel power VDMOSFETs“ *Microelectron. Reliab.*, vol. 45, pp. 1343-1348, 2005

[21] I. Manić, D. Danković, A. Prijić, Z. Prijić, N. Stojadinović, „Measurement of NBTI Degradation in p-channel Power VDMOSFETs“, Informacije MIDEM, *J. of Microelectron., Electronics Components and Materials*, vol. 44, no. 4, pp. 280-287, 2014.

[22] N. Kawai, Y. Dohi, N. Wakai, „Study for pulse stress NBTI chracteristics degradation stress“, *Microelectron. Reliab.*, 2009, vol. 49, pp. 989-993

[23] H. Reisinger, T. Grasser, W. Gustin and C. Schlünder, „The statistical analysis of individual defects constituting NBTI and its implications for modeling DC- and AC-stress“, in Proc. IEEE Int. Reliab. Phys. Symp. (IRPS2010), Anaheim, CA, 2010, pp. 7-15.

[24] I. Manić, D. Danković, V. Davidović, A. Prijić, S. Djorić-Veljković, S. Golubović, Z. Prijić and N. Stojadinović, „Effects of Pulsed Negative Bias Temperature Stressing in p-Channel Power VDMOSFETs“, Facta Universitatis, Series: Electronics and Energetics, vol. 29, no. 1, pp. 49-60, 2016.

[25] X. Ye, K. Zhang, C. Chen, Z. Li, Y. Wang, and G. Zhai, „The threshold voltage degradation model of N Channel VDMOSFETs under PBT stress“, *Microelectron. Reliab.*, vol. 91, pp. 46–51, 2018

[26] A. G. Khovanski, *Geometry of Differential Equations*, American Mathematical Soc., 1998

ABSTRACT

This paper gives insight in analysis and modeling of instability of threshold voltage shift in p-channel VDMOS power transistor IRF9520 subjected to negative bias temperature stressing. Elemental circuit for modeling of both static and pulsed stress is designed and presented, together with calculation of key parameters of the circuit. Comparison between static and pulsed modeling is discussed.

Modeling of NBT stress induced threshold voltage shifts in p-channel power VDMOSFETs

Nikola Mitrović, Danijel Danković, Zoran Prijić, Ninoslav Stojadinović

Development of Testing Environment for a Discrete D/A Converter Using NI High-Speed M Series Acquisition Device

Anđela Jovanović, Miljana Milić and Marko Dimitrijević

Abstract – **A testing environment for the D/A converter board is suggested in this paper. The system required hardware-software co-design. It is intended for the demonstration purposes at the Course of Electronic circuit testing and diagnostics and enables students to study effects of different types of defects that could appear in one mixed-signal circuit. Necessary testing signals are applied from the computer, via the acquisition device to the inputs of the converter, and obtained voltage levels at the output of the D/A converter are measured and recorded for further analyses. The software part is realized using LabVIEW programming tool.**

Index Terms – **D/A converter, acquisition device, LabVIEW.**

I. Introduction

A digital-to-analog converter (DAC) is an integrated or a discrete circuit that converts a digital number into an appropriate value of voltage or current [1]. DACs are used to control devices that require a range of voltages or currents such as electro-acoustic transducers (speakers), some types of variable-speed motors, and many other applications. A widespread usage of DACs is for waveforms creation from digital signals – for example in CD players [2].

In the first years of testing, numerical values obtained from different instruments were handwritten on a paper, in order to analyze the results off-line. The paper was the easiest medium for a real-time display of measured signals. Advances in technology, eventually, enabled the tape recording of measurements' results in the form of continuous chart using a pen. By the end of the 1980s paper-based and magnetic tapes and charts were the most popular recording methods for the scientific data [3].

In the early 1960s, before the appearance of the first personal computer (PC), the IBM company has introduced computers that were particularly developed for scientific data recordings. This was enabled by IBM 7700 Data Acquisition System as well as the later IBM 1800 Data Acquisition and Control System [4]. These systems were very expensive and massive and required significant programming and organization to perform well. However, they were all forerunners of today's PC-based data acquisition systems.

Further advances in this field were made in the mid-1980s, when the National Instruments Corporation released to the market some data acquisition cards and analog-to-digital converter boards (DAQ board) that could be combined with a low-cost personal computer [4]. Beside the application of a PC as a data acquisition platform, the most important software program that enabled programming and functioning of such systems was LabVIEW, released in 1986 for Macintosh personal computers [5]. The LabVIEW enabled engineers to program in a graphical environment and develop their specific DAQ system. LabVIEW also offered many built-in functions necessary for data processing, data analysis and data display in real-time on the computer's monitor. In 1992 National Instruments released a version of LabVIEW for graphical operating systems such as Microsoft Windows and that compatibility is still maintained.

Scientists and engineers use data acquisition systems in their laboratory research, industrial control, test and measurement. A data acquisition and control system typically consist of the followings:

- Sensors, which measure physical variables such as temperature, strain, pressure, flow, force and motion (displacement, velocity and acceleration).
- Signal conditioning part, that converts the sensor outputs into signals readable by the analog input board (A/D) in the PC.
- An analog input (ADC) board, to convert these signals into digital format usable by the PC.
- A computer with the appropriate application software to process, analyze and log the data to disk. Such software may also provide a graphical display of the data.
- An output interface, to provide an appropriate process control response.

In this paper, we will suggest a specific testing environment i.e. acquisition system for performing different tests of the digital-to-analog converter, that uses a specific NI High-Speed M Series Acquisition Device [6]. The paper is organized as follows. The following section gives a short overview of the testing methods that apply to DACS. After that, a testing hardware will be suggested and described. A corresponding software part of the testing environment will be explained next. The paper ends with the interpretation of the testing results, followed by the concluding remarks.

II. Testing of the DAC

DC performance test is the first test that should be applied when verifying the functionality of the DAC [7]. The test checks for a steady linear response. A DC performance test setup is shown in Fig. 1. The signal source generates a ramp that performs voltage level and timing signal conditioning,

Anđela Jovanović, Miljana Milić and Marko Dimitrijević are with the Electronics Department of Faculty of Electronics, University of Nis, Aleksandra Medvedeva 14, 18000 Nis, Serbia (e-mail: andjela.andjix@elfak.rs, miljana.milic@elfak.ni.ac.rs, marko.dimitrijevic @elfak.ni.ac.rs).

and such ramp is delivered to the digital pin. A voltage ramp is generated at the DAC analog output by applying the corresponding sequential digital vectors. The output voltage is then digitized in order to enable efficient analysis of the response using the test system's Digital Signal Processor (DSP). The DSP subtracts the digitized DAC output from a calculated ideal value, and the obtained difference can be used to evaluate the DAC's DC performance.

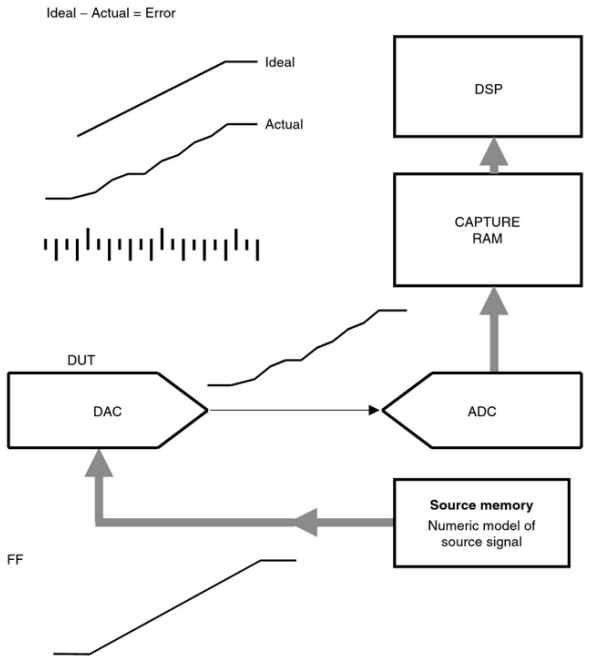

Fig. 1. A basic test setup for testing the DC performance of a DAC

The DAC's resolution can be defined as the number of different output voltage levels that it produces [7]. For example, a DAC with a resolution of 12 bits will be capable of producing 2^{12} or 4,096 different voltage levels at its output, while the DAC with a 16 bits resolution can generate 2^{16} or 65,536 different levels at its output. The resolution of the test system must overperform the resolution of the device under test when testing the accuracy of each DAC output voltage.

There are two general categories of DC tests for DAC devices [7]. The first category evaluates the device minimum and maximum output levels, referenced to an absolute specification. The offset is defined as the minimal output level, while the gain is defined in relation to the overall output signal span - from the minimum to the maximum. The second category of DC tests evaluates the device linearity, according to a relative step size value that is calculated per device. Because of the process variations, the overall analog output span may exhibit variations from one device to another. Two otherwise identical devices may be perfectly linear, but with different overall output span from the minimum to the maximum different endpoints and step size values.

The DAC offset is defined as the difference between the ideal and actual analog output for a "zero code" digital input [7]. Some devices have a correction circuit to adjust offset voltage. The offset may be tested as a worst-case measurement when the correction circuit is disabled. The offset testing implies measurement of the analog output generated by the "zero code" input and comparison of the obtained value against the fault free case. Offset may be specified as a voltage, or a fraction of an ideal LSB step, or a percentage of the ideal reference level or FSR (Full-Scale Range). The example of the offset test plot is shown in Fig. 2.

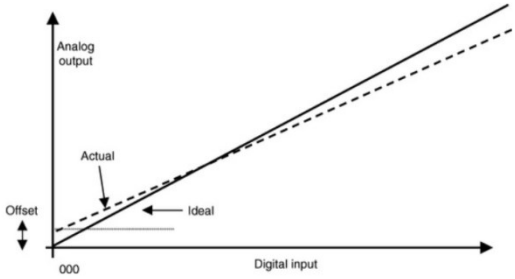

Fig. 2. Offset test plot

Gain is defined as the difference between the ideal and actual span of analog output values corresponding to the full range of digital input codes [7]. Because the total number of analog steps is $2^N - 1$, the ideal span is equal to the reference level (FSR), minus 1 ideal LSB step. The ideal LSB is equal to reference level divided by 2^N, so the span can be calculated as:

$$Reference\_level \times \left(\frac{2^N - 1}{2^N}\right) \quad (1)$$

The test procedure has to enable measurement of both the minimum output level (at "all zeroes"), and the maximum output level (at "all ones"), in order to determine the output span. The difference between the minimum and maximum output levels is specified as the device gain. DAC gain can be either positive (greater than the ideal), or negative (less than the ideal). The example of the gain test plot is shown in Fig. 3.

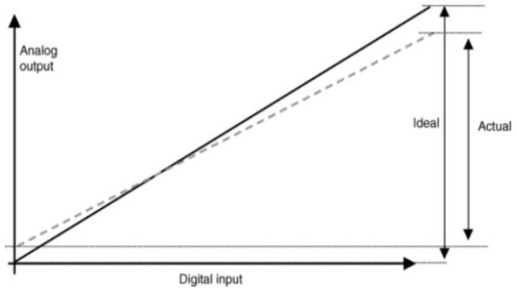

Fig. 3. Offset test plot

Ideally, each step of the DAC digital input value would increment the DAC analog output by exactly one step [7]. In an actual device, the analog step size varies. The range of the DAC describes the range of values from the minimum digital code (offset) to the maximum digital code (full scale). Linearity tests evaluate the transfer function (dependence of the output voltage levels from the input codes) based on the measured endpoints. The device LSB step is calculated by dividing the measured span of the DAC

by the number of possible input codes, as follows:

$$DeviceLSB = \left(\frac{Voltage[2^N-1]-Voltage[0]}{2^N-1}\right), \quad (2)$$

where Voltage[N] indicates the device analog level with an input code of N.

Differential Nonlinearity (DNL) is defined as the difference between the actual step size and the calculated step size [7]. Integral Nonlinearity (INL) represents the worst-case variation in any of the analog output values with respect to an ideal straight line drawn through the endpoints of the I/O graph [7]. INL is also sometimes defined in comparison to a "best fit" straight line. The illustration of the differential and integral nonlinearities is shown in Fig. 4.

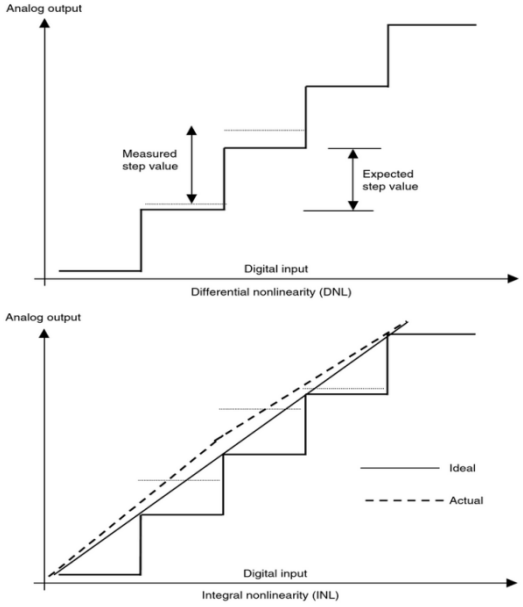

Fig. 4. Differential and integral nonlinearity

If only the DNL is tested, then each step could be "in spec", but the accumulated error could be excessive as compared to a straight-line transfer curve. If only INL is tested, then the device response according to a straight-line transfer curve could be acceptable, but each code step could exhibit excessive variation.

III. System Hardware

Digital to analog converter is used to generate analog voltage values that correspond to an input digital data [8]. Data in binary digital form can be converted into the corresponding analog form i.e. voltage value using a R-2R ladder (binary weighted resistor) network and a summing amplifier. In a mixed-signal system (analog and digital), a reconstruction (low-pass) filter at the output is used to smoothen the analog signal at the output of the DAC. The topology of such DAC circuit is shown in Fig. 5.

A basic R–2R resistor ladder network is shown in Fig. 6. Bit a_{n-1} (most significant bit, MSB) through bit a_0 (least significant bit, LSB) are driven simultaneously from a register circuit. Ideally, the input bits toggle between V = 0 (logic 0) and V = V_{ref} (logic 1). The R–2R network determines how much these digital bits contribute by their weights to the value of output voltage V_{out}. Depending on the input digital word, the output voltage (V_{out}) will have a corresponding discreet value between 0 and V_{ref} minus the value of the minimal step, corresponding to bit 0.

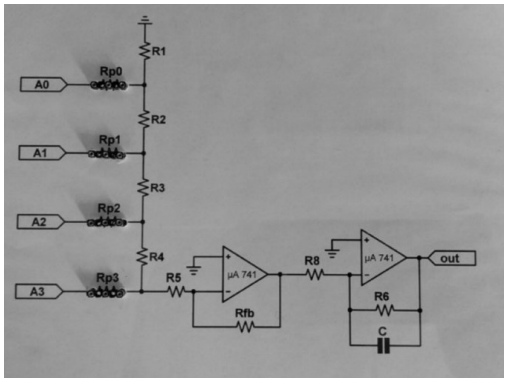

Fig. 5. Digital to analog converter using R-2R ladder network and summing amplifier, with reconstruction filter at the output

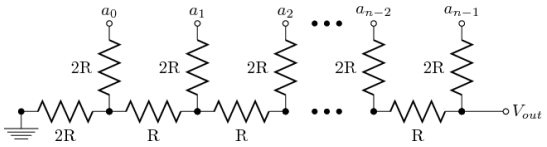

Fig. 6. n-bit R–2R resistor ladder

For a digital value VAL, of a R–2R converter with N bits and 0 V/V_{ref} logic levels, the output voltage V_{out} can be calculated as (3):

$$V_{out} = V_{ref} \times \frac{VAL}{2^N} \quad (3)$$

In this case, if N = 4 (hence 2^N = 16) and V_{ref} = 3.3 V (typical CMOS logic 1 voltage), then V_{out} will vary between 0 volts (VAL = 0 = 0000_2) and the maximum (VAL = 15 = 1111_2):

$$V_{out} = 3.3V \times \frac{15}{2^4} = 3.09375V \quad (4)$$

with steps (corresponding to VAL = 1 = 0001_2):

$$\Delta V_{out} = 3.3V \times \frac{1}{2^4} = 0.20625V \quad (5)$$

Testing of the DAC can be performed by introducing catastrophic defects i.e. by changing the input resistances Rp_0, Rp_1, Rp_2 and Rp from zero to an indefinite value[3], and by recording the transfer curves for different cases. The defects can be categorized as parametric i.e. soft, or catastrophic i.e. hard. By observing the corresponding response of the DAC, one can learn about the effects of such defects to the shape of the transfer curve, linearities and accuracy of similar circuits.

IV. Software

LabVIEW programs are often referred to as virtual instruments, or VIs, because their appearance and operation imitate physical instruments, such as oscilloscopes and

multimeters. LabVIEW contains a comprehensive set of tools for acquiring, analyzing, displaying, and storing data, as well as tools for code troubleshooting.

NI High-Speed M Series is a high-speed multifunction data acquisition (DAQ) device that uses NI LabVIEW-based software instruments [9], which allows measuring and analyzing of real-world signals. This device provides up to: 8 analog inputs (differential, or 16 single-ended), 2 analog outputs, 48 digital inputs and outputs, 2 counters, power supplies, NI-PGIA 2 and NI-MCal calibration technology for improved measurement accuracy on a compact USB device.

Each VI has two components:

- Front panel, that is containing a GUI of the VI.
- Block diagram, serving as a work-space for graphical programming.

The user interface is shown in Fig. 7. When VI is created, it has a blank front panel by default. Afterwards, control and indicator elements are added to define the inputs and outputs of the system. In this case, the VI consists of several parts: STOP control which stops the virtual instrument, Boolean indicator for binary input, and a XY graph that displays the transfer curve of the DAC.

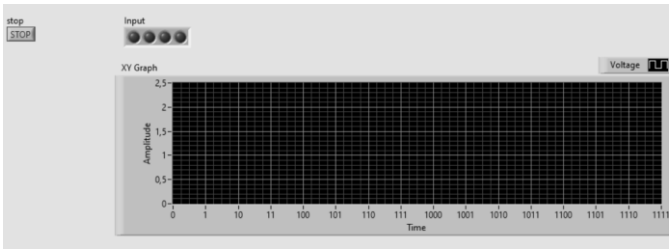

Fig. 7. User interface – front panel view

The block diagram contains the graphical source code of a LabVIEW program and it's shown in Fig. 8.

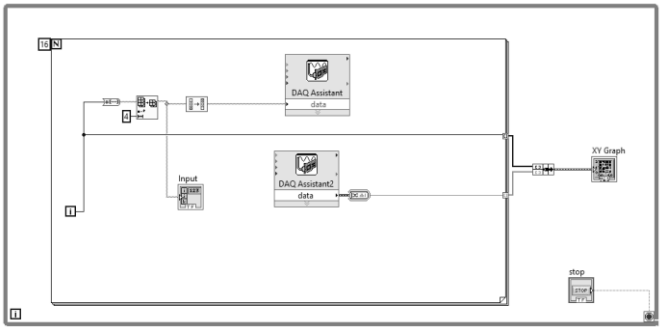

Fig. 8. Main thread – block diagram view

The concept of the block diagram is intended to separate the graphical source code from the user interface in a logical and simple manner. Front panel objects appear as terminals on the block diagram. Terminals on the block diagram reflect the changes made to their corresponding front panel objects and vice versa.

V. Results

The correctness of the realized circuit is determined by putting the actual circuit into operation. Physical realization of the project and the results of measuring are shown in figure 9. A part of a mock-up of the converter circuit is shown in Fig. 5. Some of the resistors from the schematic could be replaced with wires or left unconnected or varied in order to imitate the presence of the fault in the circuit. Each measurement implies graphical representation of the transfer curve that can be further analyzed for assessing the performance of the converter or studying the effects of different defects in the circuit.

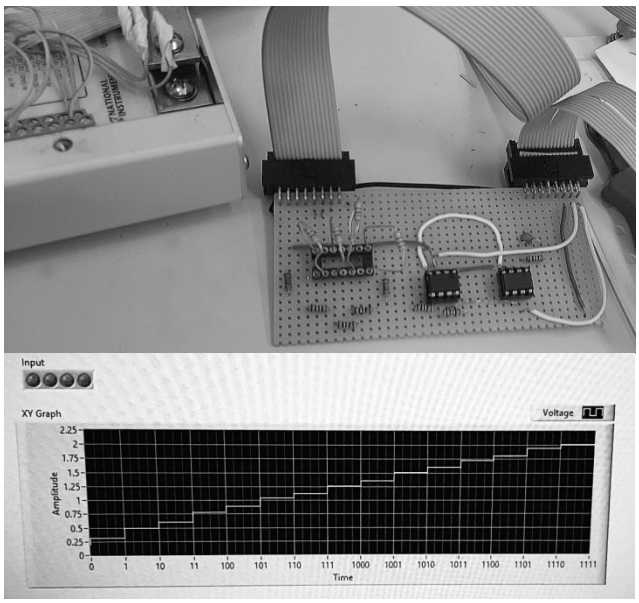

Fig. 9. D/A converter PCB connected with the DAQ and results of measuring

VI. Conclusion

The aim of the paper was to implement and study the operation of D-to-A converters as well as the effect of different types of defects, that could appear in this circuit. It is intended for educational purposes. It is supported by hardware and software co-design, and will be used for conducting laboratory excesses in Mixed-signal circuit testing.

References

[1] M. Gustavsson, J. Wikner, and N. Tan, CMOS data converters for communications. Springer Science & Business Media; 2000

[2] J. Watkinson, The art of digital audio, Taylor & Francis, 2001.

[3] M. Kimizuka, "Historical Development of Magnetic Recording and Tape Recorder", National Museum of Nature and Science Tokyo, 2012, 17.

[4] P.E. Ceruzzi, E. Paul, and W. Aspray, A history of modern computing. MIT press; 2003.

[5] S. Sumathi, P. Surekha, and P. Surekha. *LabVIEW based advanced instrumentation systems*. Vol. 728. Berlin: Springer, 2007.

[6] M. Milić, "Practicum of laboratory exercises in electronic circuit testing (in Serbian)", University of Niš, Faculty of Electronic Engineering 2019.

[7] M. Baker, "Demystifying Mixed-Signal Test Methods", Elsevier Science, 2003.

[8] H. Austerlitz, "Data Acquisition Products Using PCs", Second Edition, 2003

[9] National Instruments High-Speed M Series Multifunction DAQ for USB Product Datasheet.